

A multivariate statistical model of extreme events: an application to the  
Catalan coast

J. Lin-Ye<sup>a,1,\*</sup>, M. Garcia-Leon<sup>a</sup>, V. Gracia<sup>a</sup>, A. Sanchez-Arcilla<sup>a</sup>

<sup>a</sup>Laboratory of Maritime Engineering, Barcelona Tech, D1 Campus Nord, Jordi Girona 1-3,  
08034, Barcelona, Spain

---

**Abstract**

Wave extreme events can be understood as the combination of storm-intensity, directionality and intra-time distribution. However, the dependence structure among these factors is still unclear. A methodology has been developed to model wave-storms whose components are linked together. The model is composed by three parts: an intensity module, a wave directionality module, and an intra-time distribution module. In the Storm-intensity sub-model, generalized Pareto distributions and hierarchical Archimedean copulas have been used to characterize the storm energy, unitary energy, peak wave-period and duration. In the Directionality and the Intra-time sub-models, the wave direction (at the peak of the storm) and the storm growth-decay rates are linked to the variables from the intensity model, respectively. The model is applied to the Catalan coast (NW Mediterranean). The outcomes denote spatial patterns that coincide with the state of knowledge. The proposed methodology is able to provide boundary conditions for wave and near-shore studies, saving computational time and establishing the dependence of the proposed variables. Such synthetic storms reproduce the inter-variable co-dependence of the original data.

*Keywords:* wave storms, Catalan coast, von Mises distribution, multivariate logit function, hierarchical Archimedean copula, generalized Pareto distribution

---

**1. Introduction**

2 Wave storms strongly perturb the state of coastal environments, becom-  
3 ing such changes concomitant with episodic coastal hazards such as coastal  
4 flooding and erosion. These extreme phenomena drive complex hydrodynamic  
5 processes whose understanding is paramount for proper infrastructure design  
6 (Goda, 2010). The conventional approach is usually based on the probabilistic  
7 definition of a single parameter, typically the wave height. Other concurrent

---

\*Corresponding author  
Email address: [jue.lin@upc.edu](mailto:jue.lin@upc.edu) (J. Lin-Ye)

8 components as the duration of the storm, the storm total energy and the as-  
9 sociated wave period influence the final response of a beach or the damage  
10 evolution of a structure (Martin-Soldevilla et al., 2015; Melby and Kobayashi,  
11 2011). These variables are known to be semi-dependent (Salvadori et al., 2007;  
12 de Waal and van Gelder, 2005), but the classical methodology either a) assumes  
13 one variable to be stochastic and the other ones to be deterministic or, b) as-  
14 sumes all variables to be stochastic but completely independent. In the latter  
15 case, the lack of dependence structure hampers finding sets of physically plau-  
16 sible storm components, and requires expert guidance plus local knowledge to  
17 discern the suitable combinations.

18 A common modelling approach is to hindcast high energy events or to syn-  
19 thesize storms to a representative extreme sea-state, which is generally predis-  
20 posed by the degree of knowledge of the area. For the latter case, dependency  
21 structures among the hydrodynamic variables pose a hurdle, as they tend to  
22 be unknown. Exploratory methods, such as 2D scatter plots, have been widely  
23 used as a rule-of-thumb for the most frequent problem, wave-height vs. wave-  
24 period. However, the interpretation of existing co-dependences among several  
25 variables is challenging. Recurrently, a wide scatter cloud can mislead about  
26 biased co-dependence structures, due to subjective criteria. Storm modelling  
27 requires to consider a multivariate analysis of storm parameters (Corbella and  
28 Stretch, 2012), as univariate analyses may oversimplify coastal processes, often  
29 leading to over or under-estimation of the storm induced damages.

30 Specialized statistical techniques such as copulas can be used for finding  
31 existing relationships among storm variables (Genest and Favre, 2007; Trivedi  
32 and Zimmer, 2007) with more objective criteria. Copulas were once described  
33 by Sklar (1959), for bivariate models. They were popularized in the 1990s  
34 in financial, insurance, econometrical, risk management and actuarial analy-  
35 ses (Cherubini et al., 2004). Applications can also be found in hydrology (De  
36 Michele and Salvadori, 2003; Salvadori and De Michele, 2004) and more recently,  
37 in coastal engineering (Corbella and Stretch (2012); Wahl et al. (2011); among  
38 others).

39 Corbella and Stretch (2012) employed copula based return-periods to iden-  
40 tify the most probable combination of wave-height, wave-period, storm-duration,  
41 and water-level for a given probability of exceeding at South Africa. The thresh-  
42 old in the peak-over-threshold method was defined as a critical layer of multiple  
43 dimensions that prescribe both a safe and a super-critical combination of storm  
44 conditions. In the study, the extreme events were fitted to Generalized extreme  
45 value distributions (GEVD). They also noted the importance that their statisti-  
46 cal model was constrained, to avoid unrealistic results. Hence, they proposed  
47 wave steepness as a restriction that can increase model rigidity and enhance  
48 system robustness.

49 Li et al. (2014) fitted maximum significant wave height, peak-wave-period  
50 and storm-duration measured in the Dutch Coast with Generalized Pareto dis-  
51 tributions (GPD). They had used the Kolmogorov-Smirnov and the Chi-square  
52 tests to evaluate the goodness-of-fit. A similar approach had also been followed  
53 by Corbella and Stretch (2013). Salvadori et al. (2014), on the other hand, fit-

54 ted the significant wave-height and the duration to a Generalized Weibull model  
55 (GW) distribution and used Akaike Information Criterion (AIC) to select the  
56 suitable copula.

57 Wahl et al. (2012) applied fully nested Archimedean copulas to consider both  
58 storm surge parameters (defined with the highest turning point and the inten-  
59 sity) and the wave height, at the German coast. Nested copulas can characterize  
60 multivariate random variables by determining *a priori* nesting architecture that  
61 composes simpler copulas structures into larger and more complex ones. Wahl  
62 et al. (2012) firstly characterized the highest turning point and intensity; and  
63 then incorporated the significant wave height.

64 The main objective of this paper is to propose a methodology for inferring  
65 multivariate wave storm parameters that shares a common structure. To this  
66 aim, one of the main points of the paper has been to propose a dependence  
67 structure that links the parameters that explain wave storms. The paper is  
68 divided into two steps: Model building and Applicability. The proposed wave  
69 storm model has been split into three modules: intensity, wave directionality  
70 and intra-time storm distributions. This methodology has been tested on the  
71 Catalan coast, a fetch limited environment.

72 The structure of the paper is as follows: Section 2 deals with the methods  
73 for building the proposed statistical model. Section 3 presents the study area  
74 and, section 4, the database used. Results are summarized in Section 5 and  
75 discussed in Section 6. Finally, Section 7 sets out the conclusions.

## 76 2. Methods

### 77 2.1. Storm definition and variables

78 The determination of storms has three criteria: 1) intensity definition and  
79 associated threshold, 2) minimum time-lapse between storms ( $D_{min}^*$ ), and 3)  
80 minimum duration of the storm ( $D_{min}$ ). Wave storms are extreme phenomena  
81 that can be dealt with the peak-over-threshold description (Embrechts et al.,  
82 1997). The threshold separates storm conditions from non-storm conditions.  
83 The  $D_{min}^*$  helps satisfy independence of the samples. The independence is one  
84 part of the “independent and equidistributed” assumption for data in many  
85 statistical techniques.  $D_{min}$  discards the storms of insufficient duration and  
86 which are, therefore, of lesser significance.

87 Eastoe et al. (2013) associates the threshold with the percentile 90 of the  
88 wave height. In our paper, a different approach is proposed. The occurrence in  
89 time of extreme events, for any given geographical location, follows a Poisson  
90 distribution. Therefore, it can be deduced that the time lapse between storms  
91 must be approximately an exponential distribution; if not, these events are not  
92 extreme. Apart from this, the threshold should belong to the linear segment  
93 of a mean-excess wave-height function (Ortego et al., 2012). At the same time,  
94 the events must be statistically significant in number. The wave-height thresh-  
95 old has been varied ranging from 1.5m to 3m, whose minimum doubles the  
96 mean wave heights (CIIRC, 2010). The finally selected value of the wave-height  
97 threshold is exposed in Section 5 and discussed in Section 6.

98 Turning to the independence and equal distribution of storm samples, neigh-  
 99 bouring storms are clustered if the  $D^*$  that separates them is below  $D_{min}^*$ , which  
 100 means that both episodes belong to the same storm event. After clustering, each  
 101 storm can be considered to be independent from the others. On the other hand,  
 102 it is assumed that the marine extreme events are generated by a limited subset  
 103 of synoptic conditions (Lionello, 2012), which is true in Western Europe (Mazas  
 104 et al., 2014). Therefore, the storms are regarded as identically distributed.

105 Three candidates for  $D_{min}^*$  are proposed: 72hrs, 48hrs, and 12hrs.  $D_{min}^* =$   
 106 72hrs is because the two sub-storms in a twin storm tend to be less than 72hrs  
 107 apart. Approximately 20 – 30% of the total storm events on the Catalan coast  
 108 are twin, depending on the location (Wojtanowicz, 2010). The consideration  
 109 of  $D_{min}^* = 48hrs$  is conceptually similar to Tolosana-Delgado et al. (2011),  
 110 whereas  $D_{min}^* = 12hrs$  is based on direct observations of Catalan sea-storms.  
 111 A sensitivity test is performed to select the most correct  $D_{min}^*$  value. The test  
 112 consists of representing storms for different values of  $D_{min}^*$ . The  $D_{min}^*$  selected  
 113 and the reasons leading to this choice are stated in the Section 5 and discussed  
 114 in the Sub-section 6.1.

115  $D$  is the duration of the event between the first and last threshold crossing  
 116 (Fig. 1a). It is not to be confounded with  $D^*$ . The value of  $D_{min}$  is given in  
 117 Section 5.

118 From each independent storm, the total storm-energy ( $E$ ), the maximum  
 119 storm-unitary-energy ( $E_{u,p}$ ), the peak wave period ( $T_p$ ), the duration  $D$ , the  
 120 direction of the peak-wave ( $\theta_p^*$ ), the growth-rate and the decay-rate are obtained.

121 The Storm-intensity sub-model includes  $E$ ,  $E_{u,p}$ ,  $T_p$ , and  $D$ .

122 The  $E$  is defined as

$$E = \int_{iniT}^{endT} H_{m0}^2 dt, \quad (1)$$

123 where  $H_{m0}$  is the spectral significant wave-height, and  $t$  is time. In case that  
 124 the wave-height returns below the threshold, during the event, the duration and  
 125 the energy of these low intensity periods are included in the sums of  $D$  and  $E$ .

126 It has been highlighted in Sánchez-Arcilla et al. (2014) that the capture with  
 127 numerical models of the peak-wave-height lacks of exactitude, whereas a better  
 128 skill is found for the existing temporal trend. Therefore, a new definition of the  
 129 maximum wave-height ( $H_{max}$ ) is proposed through the definition of  $E_{u,p}$ :

$$E_{u,p} = \max_i \left( mean \left( E_{u,(i-1)} + E_{u,i} + E_{u,(i+1)} \right) \right), \quad (2)$$

130 where  $E_u$  is the unitary storm-energy at each hour. The square root of  $E_{u,p}$  is  
 131 proposed, here, as an improved definition of  $H_{max}$ , and is herein called  $H_{max}^*$ .

132 The  $H_{max}^*$  synthesizes the energy shortly before and after the peak. The  
 133 subset (see Fig. 1b) presents a) point ( $t - 1$ ): growing to reach the peak, b)  
 134 point ( $t$ ): Storm peak and c) point ( $t + 1$ ): decreasing or maintaining. The  
 135 differential energy at ( $t + 1$ ) in decreasing or maintaining the energy is a crucial  
 136 assumption for point  $t$ . The reason is that Mediterranean storms usually present  
 137 a sharp gradient during wave height growth and a milder one during decay. The

138 variables  $E$  and  $H_{max}^*$  provide more complete metrics for the storm hazard  
139 rather than a representative wave height, as they describe the behaviour of the  
140 entire storm, rather than a snapshot.

141 The  $T_p$  relates to the frequency in which the peak of the energy from the  
142 directional wave spectrum is located (Holthuijsen, 2007). The  $T_p$  of our wave-  
143 model is the value of the  $T_p$  when  $E_u$  takes the  $E_{u,p}$  value. The  $T_p$  does not  
144 vary much during each storm and its standard deviation is generally small. The  
145 reason of such reduced variation is a fetch-limited condition of the study area  
146 plus the ephemeral intensity of the storms.

147 The directionality is represented by the Directionality sub-model, and it is  
148 parameterized with the wave-direction of the storm-peak ( $\theta_p^*$ ). The value of  $\theta_p^*$   
149 is assumed to be constant throughout each individual storm-event. Both  $T_p$  and  
150  $\theta_p^*$  are values at the  $H_{max}^*$ , as interest is herein put on the behaviour of the most  
151 extreme conditions, rather than on the rest of the storms.

152 Milder slopes during decay have relevant consequences. For example, con-  
153 sider an emerged dune that collapses at the exact moment of the storm peak  
154 or maximum wave height. The after-effect (flooding/erosion) would not be the  
155 same if the energy started to decrease at the same rate as the storm growth.  
156 A sharp growth leads to collapse, defence impairment and the decay phase can  
157 lead to the real «infrastructure damage» (Gràcia et al., 2013). A parameter  
158 that considers that effect is sought in this study, whilst maintaining as much  
159 information of the peak as possible.

160 The storm wave evolution over threshold is modelled with either the irregular-  
161 trapezoidal or the triangular shapes (see Fig. 1c). A theoretical basis for the  
162 proposal of these two wave-height-evolution models can be found in Martin-  
163 Soldevilla et al. (2015), who conducted a shape analysis for one point at the NW  
164 Mediterranean Sea. This analysis is herein extended on a regional scale. The  
165 residuals associated with triangular and irregular-trapezoidal candidate wave-  
166 height-evolution models have been computed. The area below the hindcasted  
167 wave-height-evolution function has been compared to the area below each one of  
168 the candidate wave-height-evolution models. The area below the wave-height-  
169 evolution model is computed with the area within each figure plus the area  
170 below the threshold; the maximum wave-height considered in such calculation  
171 is  $H_{max}^*$ .

172 After adopting a shape, the  $D$  provides two indicators: a) the percentage  
173 of time from the beginning of the storm to the first  $H_{max}^*$  (growth-rate), and  
174 b) the percentage of time from the last  $H_{max}^*$  to the end of the storm (decay-  
175 rate). These are the ratios growth-time/ $D$  and decay-time/ $D$ , respectively, that  
176 define the storm-shape. The growth and the decay-rates are characterized by  
177 the Intra-time-distribution sub-model.

178 The Storm-intensity sub-model might influence the Directionality sub-model  
179 and the Intra-time-distribution sub-model. Therefore, the three sub-models are  
180 inter-linked.

181 *2.2. Wave-storm model building*

182 Fig. 2 summarizes the main steps followed for the construction of the storm-  
 183 model. There are three sub-models: intensity (orange boxes), wave direction-  
 184 ality (olive green boxes) and intra-time (purple boxes). Rectangle boxes repre-  
 185 sent the inputs/outputs, whereas the parallelogram boxes represent the actions  
 186 taken.

187 The storm components have been previously defined in sub-section 2.1.

188 The thresholds for the extreme variables are defined by analysing the inter-  
 189 storm-time-lapse ( $D^*$ ) and the location of the wave-height-threshold on a mean-  
 190 excess  $H_{m0}$  plot.

191 In the Storm-intensity sub-model, the univariate probability distributions of  
 192  $E$ ,  $E_{u,p}$ ,  $T_p$ , and  $D$  are characterized by GPDs, whereas their joint structures,  
 193 at each geographical node, are described by hierarchical Archimedean copulas.  
 194 The  $\theta_p^*$ , at each node (see Fig. 9), are fit to mixtures ( $n \geq 2$ ) of von Mises distri-  
 195 butions (Barnerjee et al., 2005; Mardia and Jupp, 2009), abbreviated hereafter  
 196 as *mixture of vM*, or *movM*. From the movM at one node, the mean of each  
 197 vM distribution is considered a principal direction ( $PD_i$ ) of  $\theta_p^*$ . These  $PD_i$   
 198 constitute categories for  $\theta_p^*$ . The  $PD_i$  are linked to  $E$ ,  $E_{u,p}$ ,  $T_p$ , and  $D$  through  
 199 a multivariate logistic model, then the Directional sub-model is formed.

200 From the event-time-description associated to the Storm-intensity sub-model,  
 201 the storm growth-decay rates are defined, and linked to  $D$ , resulting in the storm  
 202 Intra-time sub-model.

203 In summary, the Storm-intensity sub-model generates synthetic  $E$ ,  $E_{u,p}$ ,  
 204  $T_p$ , and  $D$  that, once introduced into the Storm intra-time sub-model and the  
 205 Directional sub-model, generate the growth-decay rates and the wave directions,  
 206 respectively. The total set of storm variables define synthetic storms that, once  
 207 filtered, are ready for applications desired. Both the model and the SIMAR  
 208 database (see Sec. 3) are validated/compared to the buoy records. Finally, the  
 209 model-buoy validation and the SIMAR-buoy comparison are contrasted to see  
 210 what kind of residual is introduced in our final model.

211 *2.3. Storm-intensity sub-model*

212 *2.3.1. Univariate marginal distribution: GPDs*

213 The  $E$ ,  $E_{u,p}$ ,  $T_p$  and  $D$  are sea dynamic variables that take positive real  
 214 values; consequently, they can be log-transformed to avoid scale effects. One of  
 215 the most widely used distributions to characterize wave peaks in a peak-over  
 216 threshold (POT) approach is the GPD (Coles, 2001). It is assumed that the  
 217 events are time points which have an associated random magnitude, and they  
 218 also must be independent and identically distributed (Coles, 2001; Tolosana-  
 219 Delgado et al., 2010). If  $X$  is the magnitude of an event and  $x_0$  is, at the same  
 220 time, a value of the support of  $X$  and a threshold, the excess over the threshold  
 221  $x_0$  is  $Y = X - x_0$ , conditioned to  $X > x_0$ . Therefore, the support of  $Y$  is either  
 222  $[0, y_{sup}]$  or a positive real line. The GPD cumulative function is

$$F_Y(y|\beta, \xi) = 1 - \left(1 + \frac{\xi}{\beta}y\right)^{-\frac{1}{\xi}}, \quad 0 \leq y \leq y_{sup}, \beta \geq 0, \xi \in \mathbb{R}, \quad (3)$$

223 and the associated probability density function is

$$f_Y(y|\beta, \xi) = \frac{1}{\beta} \left(1 + \frac{\xi}{\beta}y\right)^{-\frac{1}{\xi}-1}, \quad 0 \leq y < y_{sup}, \beta \geq 0, \xi \in \mathbb{R}, \quad (4)$$

224 where  $\beta$  is the scale parameter and  $\xi$  is the shape parameter.  $\xi$  determines  
 225 the domain of attraction of the distribution. For  $\xi < 0$ , the distribution belongs  
 226 to the Weibull domain of attraction, and the support of  $y$  is limited, being  
 227  $\left[0, y_{sup} = -\frac{\beta}{\xi}\right)$ . For  $\xi > 0$ , the domain of attraction is Fréchet, and the support  
 228 of  $y$  is  $[0, +\infty)$ . When  $\xi = 0$ , the support is infinite and the distribution belongs  
 229 to the Gumbel domain of attraction (Coles, 2001; Tolosana-Delgado et al., 2010).  
 230 The selection of a physically justified threshold for each variable enhances tail  
 231 convergence.

232 Thresholds have been defined for the GPD of each variable.  $D_{min}$  is 6hrs,  
 233 then the threshold of  $D$  is set as  $D_{min}$ , the threshold of  $E$  is computed from  
 234  $H_0^2 \cdot D_{min}$ , and the threshold of  $E_{u,p}$  is computed from  $H_0^2$ . The thresholds  
 235 for  $E$  and  $E_{u,p}$  are based on their definition. The relationship of  $H_{m0}$  to the  
 236 most widely used significant wave-height ( $H_s$  or  $H_{1/3}$ ) is  $H_{m0} = H_{1/3}/0.95$ ,  
 237 (Holthuijsen, 2007). The relationship of  $T_p$  with  $H_{1/3}$  can be approximated  
 238 by a linear expression, defined in CIIRC (2010), so the threshold of  $T_p$  can be  
 239 directly computed from the wave-height threshold.

### 240 2.3.2. Dependence structure: the Hierarchical Archimedean Copulas (HAC)

241 The set of storm components has passed a multivariate independence test  
 242 based on the empirical copula process (Genest and Remillard, 2004). This test  
 243 provides insight into inter-dependencies of any subsets of the variables. The  
 244 resulting graph, the dependogram, displays the subsets on the horizontal axis  
 245 and the statistic per subset (the departure from independence) on the vertical  
 246 axis. A statistic (vertical line) below the threshold value (bullets) means a  
 247 totally independent subset, whereas the length of the vertical line above the  
 248 bullet represents the degree of co-dependence of the variables in the subset  
 249 (refer to Fig. 4 for an example).

250 Once the semi-dependence is demonstrated, several methods are available  
 251 to model multivariate distributions. Hierarchical Archimedean copulas is one  
 252 of them. The copula simplifies the modelling as it estimates a multivariate  
 253 distribution once the marginal distributions of each individual random variables  
 254 are determined (Sklar, 1959). Pre-selected distributions separate the marginals  
 255 from the dependence structure between the random variables. Consequently,  
 256 the dependence modelling through copulas may be a suitable alternative for  
 257 building multivariate distributions when the marginals are known and heavy  
 258 tailed (de Waal and van Gelder, 2005). Heavy tails are present when extremes  
 259 are much more divergent from the mean than it would be expected.

260 The bivariate distribution described by Sklar can be generalized into a mul-  
 261 tivariate one. For any multivariate distribution function  $H$  with margins  $F_j$ ,  
 262  $j \in \{1, \dots, d\}$ , a copula  $C$  can be defined such that

$$H(\mathbf{x}_1, \dots, \mathbf{x}_d) = C(F_1(\mathbf{x}_1), \dots, F_d(\mathbf{x}_d)) \quad , \mathbf{x} \in \mathbb{R}. \quad (5)$$

263 Inversely, given a copula  $C$  and univariate distribution functions  $F_j, j \in \{1, \dots, d\}$ ,  
 264 an  $H$  defined by eq. 5 is a distribution function with marginals  $F_j, j \in \{1, \dots, d\}$ .  
 265 Being  $u_j = F_j$ , a  $d$ -dimensional copula is Archimedean if it admits the repre-  
 266 sentation

$$C(\mathbf{u}; \phi) = \phi^{-1}(\phi(u_1) + \dots + \phi(u_d)), \quad \mathbf{u} \in [0, 1]^d, \quad (6)$$

267 where the generator function  $\phi$  is continuous decreasing and convex, with  $\phi(1) =$   
 268  $0$ . An example of a generator function is the Gumbel generator function

$$\phi(u) = (-\log(u))^\theta, \quad \theta \in [1, \infty), \quad (7)$$

269  $u$  is the storm component, and  $\theta$  is the dependence parameter which indicates  
 270 independence when  $\theta = 1$  and total dependence when  $\theta \rightarrow \infty$ . The dependence  
 271 parameter  $\theta$  is distinguished from the peak-wave-direction  $\theta_p^*$ , in this text, by  
 272 adding an asterisk to the latter parameter. Other types of Archimedean copula  
 273 generator functions, such as Clayton and Frank, can be referred to in Wahl et al.  
 274 (2011).

275 Most common Archimedean copulas have constrained multivariate dependence  
 276 structures, as they usually depend on a single parameter of the generator  
 277 function. Moreover, they are insensitive to variable permutation, which implies  
 278 that all margins of the same dimension are equal, deeming them unable to model  
 279 asymmetries in the variable co-dependences (Hofert and Machler, 2011). Hier-  
 280 archical Archimedean copulas (HAC, see Fig. 3 for an example) can be a useful  
 281 tool to overcome these drawbacks, by nesting simple 2D-Archimedean copulas  
 282 into multilayer tree structures that are fitted in a recursive way (Okhrin et al.,  
 283 2013).

284 The hierarchical structure of the HAC provides a series of advantages: a) it is  
 285 more flexible and intuitive than the simple Archimedean copulas, b) it can model  
 286 asymmetries in the variable co-dependences, unlike simple Archimedean copulas,  
 287 c) there is a marginal cumulative distribution function at each node of the tree,  
 288 d) it requires less parameters than other kinds of copulas (e.g. elliptical copula),  
 289 and e) when basing each copula on a single generator function, the copula  
 290 parameters rise as the level increases, enabling simpler dependence analyses.

291 Different generator functions can be used to obtain the  $\theta$  at each nesting  
 292 level of a HAC. Extreme storms present a typical pattern of producing extreme  
 293 values for most storm components, such as  $E, E_{u,p}, T_p$  and  $D$  above a certain  
 294 threshold. Then, the most suitable HAC type is Gumbel (when a generator  
 295 function is used at all the levels of nesting of a HAC, this generator function  
 296 gives its name to this HAC). The Gumbel HAC includes such upper extreme  
 297 dependence (Salvadori et al., 2007). Other HACs, such as the Clayton and the  
 298 Frank HACs, may also be employed, as discussed in Wahl et al. (2012). Hence,  
 299 although the Gumbel type is selected *a priori* for this study, goodness-of-fit-tests  
 300 are also applied to Clayton and Frank HAC types, with the aim of verifying the  
 301 suitability of Gumbel.

302 The aggregation at each nesting level depends on a parameter  $\varepsilon$ . If the  
 303 absolute difference of the dependence parameters of two subsequent nodes is



304 smaller than  $\varepsilon$  (see eq. 8),

$$|\theta_1 - \theta_2| < \varepsilon, \quad (8)$$

305 the aggregation method «mean», the one used here, equates the  $\varepsilon$  to the average  
306 value between the  $\theta$ s.

307 An example of a four-dimensional HAC can be

$$C(\mathbf{u}_1, \mathbf{u}_2, \mathbf{u}_3, \mathbf{u}_4) = C_3 \{C_2(\mathbf{u}_1, \mathbf{u}_2, \mathbf{u}_3), \mathbf{u}_4\} = \phi_3^{-1} \{ \phi_3 \circ C_2(\mathbf{u}_1, \mathbf{u}_2, \mathbf{u}_3) + \phi_3(\mathbf{u}_4) \}. \quad (9)$$

308 If the copula tree (see Fig. 3) spreads its “branches” upside down, the lowest  
309 hierarchical level would be the tip of the branches. At such lowest hierarchical  
310 level, the parameter of any pair of the given variables is estimated. The couple  
311 with the strongest dependence is aggregated and substituted by a joint pseudo-  
312 variable (Okhrin et al., 2013). For example, let  $E$  and  $D$  share a common  
313 dependence parameter  $\theta_{(E,D)} = 4.44$ . Let it be the highest valued dependence  
314 parameter among all the pairs of variables. The pair of variables  $(E, D)$  can be  
315 substituted by the pseudo-variable

$$\mathbf{Z}_{(E,D)} \stackrel{def}{=} \phi_{\hat{\theta}_{(E,D)}}^{-1} \left[ \phi_{\hat{\theta}_{(E,D)}} \left\{ \hat{\mathbf{F}}_D(D) \right\} + \phi_{\hat{\theta}_{(E,D)}} \left\{ \hat{\mathbf{F}}_E(E) \right\} \right]. \quad (10)$$

316 At the next level, the parameter of all the pairs of variables and pseudo-variables  
317 are again evaluated. This procedure is continued until the highest hierarchical  
318 level (i.e. the root) is reached (see Fig. 3).

319 Several approaches can be found in the literature to determine the HAC  
320 agreement with data. Chen et al. (2004) proposed a dimension-free goodness-  
321 of-fit test which has been adapted to construct the HACs. The graphical test  
322 detailed in Okhrin and Ristig (2012) has been applied to check the goodness-  
323 of-fit at each nesting-level. It is complemented with quantitative values from a  
324 parameter  $k^2$  (Gan et al., 1991).

325 Okhrin and Ristig (2012) compares the model probability-distribution with  
326 the empirical probability-distribution. The expression of an empirical copula is

$$\hat{C}(\mathbf{u}_1, \dots, \mathbf{u}_d) = n^{-1} \sum_{i=1}^n \prod_{j=1}^d \mathbf{I} \left\{ \hat{F}_j(\mathbf{X}_{ij}) \leq \mathbf{u}_j \right\}, \quad (11)$$

327 where  $n$  is the sample size,  $d$  is the number of variables,  $\hat{F}_j(\mathbf{X}_{ij})$  is the empirical  
328 marginal distribution function of a variable  $\mathbf{X}_{ij}$ , and  $\mathbf{u}_j$  is a vector belonging  
329 to the interval  $[0, 1]$ .  $\mathbf{I}$  is a unit function (it is 1 when the argument is true, and  
330 0, when the argument is false), so that the product represents the unit function  
331 of the AND combination of all the  $j$  conditions

$$\hat{F}_j(\mathbf{X}_{ij}) \leq \mathbf{u}_j.$$

332 .  
333 Gan et al. (1991)’s  $k^2$  quantifies the agreement of the analysis at each nesting  
334 level. Each one of these levels only has two variables, then the criterion is herein

335 restricted to 1D dimension comparisons.  $k^2$  takes values in  $[0, 1]$ , the larger the  
 336 number, the highest the similarity of the vectors involved.

337 Here,  $\theta$  of different Gumbel copulas are not easily comparable, as the support  
 338 of  $\theta$  is semi-infinite. Thus,  $\theta$  are transformed into Kendall's  $\tau$ , or Kendall's rank  
 339 correlation coefficient (Kendall, 1937), the support of which is  $[0, 1]$ . The value  
 340 1 is excluded for corresponding to the infinity value in  $\theta$ .

341 Once HAC structures are obtained for each node,  $\tau_{(E,D)}$  values are obtained  
 342 through ordinary kriging (OK) (Wackernagel, 2003), along the Catalan coast,  
 343 in order to visually identify the spatial distribution of the co-dependences of  $E$   
 344 and  $D$ . This approximation remains valid for zones where the observed hydro-  
 345 dynamic patterns do not differ excessively, and offers estimations at unsampled  
 346 areas.

347 *2.4. Linking wave-direction to Storm-intensity: The wave directional sub-model*

348 It is not possible to include the  $\theta_p^*$  and the growth-decay rates into the HAC  
 349 in the Storm-intensity sub-model, since these storm-components do not have a  
 350 support in the space of the real numbers. However, according to results from  
 351 dependograms, directionality and growth-decay rates are not entirely independ-  
 352 ent from the Storm-intensity model. Therefore, the directionality and the  
 353 growth-decay rates are compelled to relate to the Storm-Intensity sub-model  
 354 via a regression model, although not through a HAC structure.

355 The standard approach transforms a continuous variable into a predefined  
 356 set of categories. Usually, the reference coordinate system (i.e. North) and  
 357 some predefined bins divide the wave-rose into 16 sectors. This poses a problem  
 358 when the wave-directions are near the boundaries between two sectors, and can  
 359 mislead regarding contingency. It is, then, crucial to select a set of categories  
 360 based on the data itself. Both reference and bin size can be established with  
 361 movM distributions. This type of distributions allow a more flexible definition  
 362 of the wave-direction contingency, as elementary distributions are not assumed  
 363 constant over preassigned subintervals. What is more, it can be transformed  
 364 into categories of principal wave-directions (PD), simplifying the prediction of  
 365 wave-directions.

366 In this methodology, wave-directions are first characterized with movM dis-  
 367 tributions (Barnerjee et al., 2005; Mardia and Jupp, 2009), whose probability  
 368 distribution function of a mixture of  $k$  elements is

$$f(x|\hat{\Theta}) = \sum_{h=1}^k \alpha_h f_h(x|\hat{\theta}_h), \quad k \in \mathbb{N}, \quad (12)$$

369 being  $x$  a circular variable, with  $\mu_h$  as the  $h$ th mean, and  $\kappa_h$  as the  $h$ th “standard  
 370 deviation”. The  $\alpha_h$  are the mixture probabilities, they are non-negative and sum  
 371 to one; by definition, the mode with the largest  $\alpha_h$  is the principal direction.  
 372  $\hat{\theta}_h = (\mu_h, \kappa_h)$  for  $1 \leq h \leq k$ , and  $\hat{\Theta} = \{\alpha_1, \dots, \alpha_k, \hat{\theta}_1, \dots, \hat{\theta}_k\}$ .  $\hat{\Theta}$  represents the  
 373 mixture probabilities, as well as the means and standard deviations of the vM  
 374 distributions in the mixture. Both  $\hat{\theta}$  and  $\hat{\Theta}$  have hats, in order to distinguish  
 375 them from the peak-wave-directions ( $\theta_p^*$ ) and HAC parameters ( $\theta$ ).

376 An Expectation maximization (EM) approach is used for maximizing the  
 377 expectation of eq. 12. With the constraints on the vMF mean and deviance,  
 378  $\mu_h^T \mu_h = 1$  and  $\kappa_h \geq 0$ , the expression of the mixture probabilities  $\alpha_h$  is:

$$\alpha_h = \frac{1}{n} \sum_{i=1}^n p(h|x_i, \hat{\Theta}), \quad n \in \mathbb{N}, \quad (13)$$

379 where  $n$  is the total number of elements in the sample,  $x$  is the angle, and  
 380  $\hat{\Theta}$  is the parameter appearing in the eq. 12, and described above.  $p(h|x_i, \hat{\Theta})$  is  
 381 the probability of appearance of the  $h$  vM distribution, given the angle  $x_i$  and  
 382 the parameter  $\hat{\Theta}$ .

383 From the soft EM framework used here, the distribution  $p(h|x_i, \hat{\Theta})$  is given  
 384 by

$$p(h|x_i, \hat{\Theta}) = \frac{\alpha_h f_h(x_i|\hat{\Theta})}{\sum_{l=1}^k \alpha_l f_l(x_i|\hat{\Theta})}, \quad (14)$$

385 where  $\alpha_h$ ,  $x_i$ ,  $k$ , and  $\hat{\Theta}$  are the same variable as in eqs. 12 and 13, and  
 386  $f(x_i|\hat{\Theta})$  is the probability distribution function of  $x_i$ , given  $\hat{\Theta}$ . The soft EM  
 387 framework, assigns soft (or probabilistic) labels to each point given by eq. 14.  
 388 Other candidates can be the hard, or “winner takes all”, EM, but the soft EM  
 389 is selected for its flexibility, in comparison with the hard EM.

390 The wave-direction is decomposed into the sine and cosine of the angle, and  
 391 these two elements are then fit by movM. The corresponding movM parameters  
 392 can be used to generate synthetic pairs of sine-cosine that can be combined  
 393 to estimate the synthetic wave-direction. The Watson’s two-sample uniformity  
 394 test then helps identifying the strictly necessary number of modes in the movM  
 395 distribution (Pewsey et al., 2013). By doing so, it improves goodness-of-fit,  
 396 whereas avoiding over-fitting. This test checks whether two groups are extracted  
 397 from a common distribution. The criterion for the goodness of fit is set as  
 398 the statistic  $U^2$  to be smaller than 0.152, which corresponds to  $p$ -value= 0.1.  
 399 When this criterion is met, it means absence of significant difference between  
 400 the empirical distribution and the model distribution.

401 The means  $\mu_k$  of each movM are considered as principal directions ( $PD_k$ ).  
 402 These  $PD_k$  delimit a set of categories. Hence, the continuous wave-direction in  
 403 each storm is labelled by a category that bonds the “influence area” of one of  
 404 the  $k$  vM distributions in the mixture. The main advantage of this approach is  
 405 that the categorization of this variable is data-dependent, so the ranks can be  
 406 related to the Storm-intensity sub-model.

407 The relationship between the predicted  $PD_k$  categories and the variables  
 408 from the Storm-intensity sub-model ( $\log E$ ,  $\log E_{u,p}$ ,  $\log T$ ,  $\log D$ ) is built with a  
 409 multinomial logistic model (Hosmer et al., 2013). A multinomial logistic model  
 410 consists of a regression model where the dependent variables (i.e.  $PD_k$ ) are  
 411 categories and the explanatory variables can be continuous. Particularly, the  
 412 predictors used in the multinomial logistic model are  $E$ ,  $T_p$  and  $D$ .  $E_{u,p}$  is not

413 non-significant as a predictor. Therefore, the multinomial model predicts the  
 414 probabilities that a particular  $PD_k$  can happen under certain intensity quanti-  
 415 ties, then joining directional patterns with its associated  $E$ ,  $T_p$  and  $D$ .

416 *2.5. Intra-time distribution sub-model*

417 This sub-model is linked with the Storm-intensity sub-model via the  $D$ .  
 418 A polynomial function is adopted; it predicts the growth-decay rates from a  
 419 given  $D$ . Other variables from the Storm-intensity sub-model do not show clear  
 420 relationship to the growth-decay rates.

421 A polynomial function is sufficiently flexible capturing the inner structure  
 422 within  $D$  intervals vs. the growth-decay rates. What is more, a suitable rela-  
 423 tionship is a third degree polynomial function, where the independent variable  
 424 is  $D$ :  $f(D) = a_0 + a_1D + a_2D^2 + a_3D^3$ .

425 *2.6. Wave storm generator*

426 Once our model is built, the applicability consists of generating synthetic  
 427 storms, whose parameters are related. These storms has been produced by  
 428 recursive simulations that consider the nested structure of the HAC model, as  
 429 well as the links between our three sub-models. The storms are generated for a  
 430 given design return periods ( $T_r$ ) until there is approximately a sample with more  
 431 than 1000 storms, at each node. The selected tolerance for the error in joint  
 432 and marginal  $T_r$ , in the storm generation, is 20%. This degree of tolerance is  
 433 suggested by an estimate of observational residuals in the Catalan Sea (Sánchez-  
 434 Arcilla et al., 2008a, 2014).

435 There is not a unique correct design  $T_r$ , since in a multidimensional space  
 436 there is no single total order. There is a variety of failure modes and diverse  
 437 probabilities of failure that combine the existing parameters. Several criteria  
 438 exist to define a multivariate ( $n$ -variate)  $T_r$  (Salvadori and De Michele, 2010),  
 439 and four representative expressions are listed below. These  $T_r$  take into consid-  
 440 eration the various storm descriptors in the Storm-intensity sub-model.

441 The Kendall  $T_r$  (Salvadori et al., 2007) is:

$$Tr_k = \frac{1}{\lambda \cdot (1 - F(\mathbf{x}))}, \quad \lambda \in \mathbb{R}, \mathbf{x} = (x_1, \dots, x_i, \dots, x_n) \in \mathbb{R}^n, \quad (15)$$

442 where  $\lambda$  is the annual occurrence of storms,  $\mathbf{x}$  is the storm components  
 443 characterized by HACs, and  $F(\mathbf{x})$  is

$$F(\mathbf{x}) = \frac{1}{n} \sum_{i=1}^n F(X_i < x_i), \quad (16)$$

444 where  $\lambda$  is the same concept as in the Kendall's  $T_r$ ,  $u_i$  is the cumulative  
 445 probability of a  $1D$ -variable,  $\mathbf{I}$  is the unit interval  $[0, 1]$ , the critical threshold  
 446  $t \in \mathbf{I}$  is given by  $t = \inf \{s \in \mathbf{I} : K_C(s) = p\} = K_C^{[-1]}(p)$ , where  $K_C$  is the  
 447 Kendall coefficient.

448 Two other possible ways to compute the joint  $T_r$  are via the mean value of  
 449 the marginal  $T_r$  (eq. 17) or the geometric mean value of the marginal  $T_r$  (eq.  
 450 18):

$$Tr = \frac{1}{n} \sum_{i=1}^n Tr_i(x) , x \in \mathbb{R}, \quad (17)$$

$$Tr = \sqrt[n]{\prod_{i=1}^n Tr_i} , x \in \mathbb{R}, \quad (18)$$

451 where  $Tr_i$  is the  $T_r$  of  $x$ .  $x$  is a storm component and  $Tr_i$  is calculated by  
 452 means of eq. 15.

453 All these different definition of  $T_r$  bring forth the need for further research  
 454 into multivariate  $T_r$ , as the currently available tools are mostly statistical the-  
 455 oretical artefacts based on the not always true assumption that high values of  
 456 variables are dangerous. All four definitions of  $T_r$  have been tested on, and,  
 457 finally, the eq. 17 is selected for presenting a better approach to physical mea-  
 458 surements. See Section 5 for results, and Section 6 for the discussion.

459 For a contingency study, the storm components are considered truncated.  
 460 So pie-charts can be applied to represent which intervals are more frequent  
 461 than others. A pie-chart leads to visually assess the different categories and  
 462 the relative weights over a total simulated number of storms. For the case of  
 463 of wave-height, the  $H_s$  are within 3 – 3.5 m, and these values constitute the  
 464 principal category. This visualization of the frequencies leads to a simple inter-  
 465 pretation of the storm component interactions among themselves, thus aiding to  
 466 find representative scenarios given a  $T_r$ . The 1, 2, 5, 10, 25 year return periods  
 467 have been selected for synthetic data clustering, as they are routine in infras-  
 468 tructure design. The life-time of a hard coastal protection infrastructure (e.g.  
 469 revetment, groyne, etc.) may be established as 25 years (DGP, 2001), whereas  
 470 soft coastal protection (e.g. nourishment, dune building, etc.) are associated  
 471 with lower  $T_r$  (5 or 10yr) (García-León et al., 2015; Sánchez-Arcilla et al., res).  
 472 Direct applications of this methodology can provide hydrodynamic loads for  
 473 infrastructure design and diagnosis.

### 474 3. Study area

475 The Catalan coast is part of the north-western Mediterranean Sea (see Fig.  
 476 5). This water body is characterized by its semi-enclosed nature, the orographic  
 477 patterns, air-sea temperature differences and the passage of low pressure centres  
 478 from the Atlantic (Lionello, 2012). The main morphological features are  
 479 the existence of mountain chains parallel and close to the coast, the Pyrenees  
 480 Mountains to the north, and the Ebre river valley to the south. These oro-  
 481 graphic discontinuities, together with the major river valleys, allow for strong  
 482 winds to be channelled down to the coast (Grifoll et al., 2015).

483 The Catalan coastal winds are typically low to medium, on average, ranging  
 484 up to 11.05m/s (Sánchez-Arcilla et al., 2008b). The most frequent and intense

485 wind is the Tramuntana (N), appearing from November to March. It has been  
486 observed that it is the major forcing for the northern and central Catalan coastal  
487 waves. From latitude  $41^\circ N$  southward, the principal wind direction is the Mis-  
488 tral (NW). It is channelled by the western Pyrenees and the Ebre valley. The  
489 NW winds are formed by the superposition of gap and downhill flows from the  
490 Pyrenees. A secondary wind mass, the Ponent, comes from the depressions in  
491 northern Europe and sweeps the entire Iberian Peninsula from west to east.

492 Eastern winds are frequent during the summer. They are commonly trig-  
493 gered by an intense high-pressure area on the British Islands. Another origin is  
494 a high level of cold air pool deepening over the Mediterranean sea, which lead  
495 to cyclo-genesis, resulting in the passage of a low off the Catalan coast (Bolaños  
496 et al., 2009; Lionello, 2012). Winds are more variable for higher intensities.  
497 Thus, some relatively large wind modulus-variability is generated during storms  
498 (Bolaños, 2004). Wave-directions are directly correlated with wind-direction,  
499 except the angle  $50^\circ$  of waves, which can be generated by winds in the sector  
500 NNW-ENE, approximately. This might be explained by the orientation of the  
501 coast-line, all winds, at some point, seems to create an alongshore wave-train.

502 The Catalan coast has a micro-tidal environment (Lionello, 2012). The slope  
503 of the bathymetry is relatively steep in the north, while it becomes milder to  
504 the south. This has a direct impact on how waves behave when reaching the  
505 coast, as the bathymetry has an effect on the type of the impacting wave, and  
506 the beach slope determines the vulnerability to flooding. Waves on the Catalan  
507 Sea also have a critical effect on sediment-transport, as the short wave-lengths  
508 do not allow the beach sediment to restore itself during summer-time.

509 For fetch limited environments, direct correlation has been observed between  
510 wind and wave-directions, this suggest that the local wind is the main forcing  
511 for waves at the Catalan Sea, rather than distant winds, so we stress on the  
512 difference between local (which generate wind-waves) and distant winds (which  
513 generate swell-waves). This reinforces the idea that storm-waves at the Catalan  
514 coast are driven by mesoscale processes that span the entire fetch, whereas the  
515 swell contributions can be considered as secondary.

516 According to Bolaños et al. (2009), who used XIOM buoy data, the largest  
517 waves come from the east, caused by the joint action of the most significant  
518 fetches and winds. In further analysis with dependograms, it can be specified  
519 that such directionality is most evident for  $\overline{T_p}$ , at almost the entire Catalan  
520 coast. The directionality of  $H_{m0}$  is limited to nodes N4, N5, C2, C4, S1 and S4.

521 The mean significant wave-height ( $\overline{H_s}$ ) is 0.72m from Barcelona city north-  
522 ward (the quantile 75 of  $H_s$  is  $q_{H_s,75} = 0.89\text{m}$ ,  $H_{s,max} = 5.85\text{m}$ ), and 0.78m  
523 southward ( $q_{H_s,75} = 0.98\text{m}$ ,  $H_{s,max} = 5.48\text{m}$ ). The extreme values are ap-  
524 proximately seven times the average values. In fact, the standard deviation is  
525 relatively high, being 30% of the mean. What can be expected is that a struc-  
526 ture can be severely challenged by storms of higher  $T_r$ . Northern storms might  
527 be slightly more hazardous, as it is observed here that  $H_{s,max}$  are 0.37m higher  
528 at northern sites than southern ones.

529 The mean peak-wave-period ( $\overline{T_p}$ ) is 5.85s on the northern Catalan coast  
530 ( $q_{T_p,75} = 6.73\text{s}$ ,  $T_{p,max} = 15.87\text{s}$ ) and 5.62s on the southern Catalan coast

531 ( $q_{T_p,75} = 6.65\text{s}$ ,  $T_{p,max} = 14.1\text{s}$ ) (CIIRC, 2010). In this case, standard deviation  
 532 is double the mean value. However, the quantile 75, the maximum and the  
 533 mean are of a similar order of magnitude. The  $T_p$ , including the mean and the  
 534 maximum values, is geographically homogeneous.

535 The NW waves are the highest in Tortosa cape, while the eastern and south-  
 536 ern waves are steepest in Llobregat delta (Bolaños et al., 2009). There is also a  
 537 weakly linear relationship between the mean wave-period ( $T_z$ ) and the  $H_s$ , that  
 538 is, for each increase in 2s of  $T_z$ ,  $H_s$  increases by 1m.

539 The study area is divided into hydro-dynamically homogeneous sectors of  
 540 similar lengths (see Fig. 5). The northern sector (N-) spans the area from the  
 541 border with France ( $42.44^\circ N$ ,  $3.18^\circ E$ ) to the Mataro Port ( $41.53^\circ N$ ,  $2.44^\circ E$ ),  
 542 the central sector (C-) extends from the Mataro Port to the Segur de Calafell  
 543 port ( $41.19^\circ N$ ,  $1.61^\circ E$ ), and the southern sector (S-) ranges from the Segur  
 544 de Calafell port to the border with the Autonomous Community of Valencia  
 545 ( $40.53^\circ N$ ,  $0.52^\circ E$ ). The sector boundaries are political frontiers and locations  
 546 of change in beach orientation. Each sector features a mean shoreline orientation  
 547 that determines “a posteriori” whether a simulated synthetic storm (see Section  
 548 2) will reach the coastline.

#### 549 4. Data source, and explanatory analysis of the storms

550 The training set that the proposed statistical model uses comes from the  
 551 SIMAR dataset (Gomez and Carretero, 2005). The data consist of wave-hindcast-  
 552 simulations by WAM (WAMDI Group et al., 1988) and WAVEWATCH3 (Tol-  
 553 man, 2009), fed with HIRLAM wind fields (Unden et al., 2002). SIMAR pro-  
 554 vides consistent, gap-less and spatially dense time series. A series of nodes are  
 555 selected to representatively cover each one of the above mentioned sectors. This  
 556 results in 6-8 nodes being assigned to each sector. N1 is near Creus Cape and  
 557 S7 is well below Ebre Delta (see Fig. 5). SIMAR nodes are located at  $-50\text{m}$   
 558 depth, which are intermediate waters, in this area.

559 The hindcast ranges from the 14<sup>th</sup> January 1996 to the 25<sup>th</sup> February 2013.  
 560 Data in some nodes extend to the 22<sup>nd</sup> January 2014. SIMAR provides a variety  
 561 of wave-spectra-parameters, such as  $H_{m0}$  and  $T_p$ , among other information,  
 562 including incoming wave direction and moment in time. The time resolution  
 563 before June 2000 is of 3hrs and changes to 1hr thereafter. Spline-interpolation  
 564 has been applied to discretize all time-series with the same temporal resolution.

565 Storms are obtained from the SIMAR dataset with the methodology de-  
 566 scribed in Section 2. Explanatory analysis shows that the quantiles 50 of  $E$ ,  
 567  $H_{max}^*$ ,  $T_p$  and  $D$  are spatially uniform, whereas their quantile 85 present more  
 568 geographical heterogeneity: higher values in the north, lower values in the south  
 569 and in the Roses Bay (see Fig. 5); specifically, the  $E$ ,  $D$ , and  $H_{m0}$  decrease ap-  
 570 proximately 25% southward and in the Roses Bay, while the  $T_p$  increases 10% in  
 571 the same direction. The Northern part of the Catalan coast (above  $41.2^\circ N$ ) has  
 572 higher waves in its strongest storms, reaching values above 4m. Storms in these  
 573 locations also have a longer  $D$ , surpassing 50hrs. The  $T_p$ , on the other hand, are  
 574 larger from  $41.8^\circ N$  southward. Note that the quantiles under 50, the quantiles

575 15 of  $E$ ,  $H_{max}^*$ ,  $T_p$  and  $D$ , for instance, are also spatially homogeneous, but they  
 576 are ignored, as they are influenced greatly by the selected GPD thresholds.

577 Both PdE («Puertos del Estado» or State harbours) and XIOM buoy records  
 578 (see Fig. 5 and table 1) are used for model validation. The selected buoys are  
 579 located at similar positions to the SIMAR nodes. XIOM buoys provide  $H_{m0}$ ,  
 580 mean wave period ( $T_m$ ), and date. For the sake of comparison with SIMAR  
 581 dataset, the relation  $T_m/T_p = 0.8$  (Goda, 2010) is considered.

## 582 5. Results

583 Figs. 6a through 6h, and Figs. 7a and 7b show a threshold iteration test  
 584 on the nearest PdE and SIMAR nodes to the Barcelona City. This location is  
 585 chosen for being the geographical centroid of the Catalan coast. The storm-  
 586 threshold is named  $h_0$ . Following to the criteria mentioned in Section 2, the  
 587 selected value for  $h_0$  is 2.2m. On the other hand, the most adequate  $D_{min}^*$  is  
 588 12hr.

589 The numbers of storms, at each node, are listed on Table 2. The northern  
 590 zone is the stormiest whereas lower number of storms were found at the south,  
 591 coinciding with the state of the art (Sánchez-Arcilla et al., 2008b).

592 The GPD threshold of  $D$  is considered to be  $D_{min} = 6$ hrs, the threshold of  
 593  $E$  is  $H_0^2 \cdot D_{min} = 29.4m^2$  hr, and the threshold of  $E_{u,p}$  is  $H_0^2 = 4.84m^2$ . The  
 594 threshold of  $T_p$  corresponding to  $H_{1/3} = 0.95 \cdot H_{m0}$  is 8.17s (CIIRC, 2010).  $E$ ,  
 595  $E_{u,p}$ ,  $T_p$  and  $D$  are well fit by GPD, with the selected thresholds (see parameters  
 596 in table 3).

597 The joint structure of the Storm-intensity sub-model is compared through  
 598 goodness-of-fit plots for the Gumbel, Clayton and Frank HACs. The three HACs  
 599 present similar qualitative behaviour and  $k^2$  parameter value. Then, the Gumbel  
 600 type HAC is selected for being able to include upper extreme dependence. The  
 601 “mean” aggregation method, in combination with the Gumbel type HAC, is  
 602 adopted, for providing the best fit.

603 Two Gumbel HAC tree types (A and B) are observed (see Fig. 3), based on  
 604 the co-dependence of  $E_{u,p}$  to  $E$  and  $D$ . Type A HAC-trees differ slightly from  
 605 type B HAC-trees. In type A trees,  $E_{u,p}$  has a stronger relationship with  $E$  and  
 606  $D$ . There is no clear spatial pattern in how A and B trees are distributed (see  
 607 table 4), but there is strong co-dependence between  $D$ ,  $E$ , and  $E_{u,p}$ ; fact that  
 608 is corroborated by the dependograms (see Fig. 4). The dependence parameter  
 609 of  $\log D$  and  $\log E$  ( $\theta_{(\log E, \log D)}$ ), or, in other words, that of  $D$  and  $E$  ( $\theta_{D,E}$ ),  
 610 is transformed into a  $\tau$  value (Kendall, 1937). This  $\tau$ , which has been called  
 611  $\tau_{(E,D)}$ , is kriged on the  $-50$ m bathymetry (see Fig. 8). It is detected that this  
 612 dependence has a tendency to decrease southward (see Fig. 8).

613 The contingency of  $\theta_p^*$  are shown on Fig. 9 and table 5. It is observed  
 614 that the principal  $\mu$  is, from N1 to N6, approximately  $330^\circ$ - $20^\circ$  (except at N3).  
 615 Central nodes (N7 to S2) are heavily influenced by easterly waves, whereas  
 616 southern nodes (S3 to S7) suffer more heterogeneous influences. The secondary  
 617 direction at N1 to S6 are eastern waves, whereas it becomes predominantly



618 southern waves from N7 southward. The wave-contingency at N3 is similar to  
619 neighbouring nodes, only that the principal and the second directions are at  
620 the opposite direction than at node N2, for instance. It is observed that most  
621 nodes have bi-modal wave-directions, coinciding with (Alomar, 2012; Bolaños  
622 et al., 2009). The coefficients of the multivariate logit function to predict  $\theta_p^*$ ,  
623 from  $\log E$ ,  $\log E_{u,p}$ ,  $\log T$  and  $\log D$ , are listed on table 6.

624 Regarding the residuals associated with the triangular and irregular-trapezoidal  
625 candidate wave-height-evolution models, both the overestimation and underesti-  
626 mation residuals are well below  $3\text{m} \cdot \text{hr}$  (that is considerably inferior to the area  
627 below the  $H_{m0}$  time-series' curve) and ranges from a quantile 10 of  $20.20\text{m} \cdot \text{hr}$  to  
628 a quantile 90 of  $157.65\text{m} \cdot \text{hr}$ . The trapezoidal model overestimates in  $0-1\text{m} \cdot \text{hr}$   
629 more than the triangular model, and the triangular underestimates in  $0-1\text{m} \cdot \text{hr}$   
630 more than the trapezoidal model. Therefore, the trapezoidal model is selected  
631 as overestimation has been considered to be less harmful than underestimation,  
632 assuming that both residuals are of the same order of magnitude.

633 The growth-decay rates are assessed with heat-maps, whose "affection areas"  
634 are defined with a bandwidth of  $radius = 5\text{hrs}$  ( see Fig. 10). When several  
635 points are inside the "affection area" of one point, the frequency for such pair-  
636 ing is higher and the area becomes "darker". The coefficients of third degree  
637 polynomial that relates  $D$  and growth are shown on table 7.

638 Our model has been validated by buoy data (see Figs. 13 and 14). Figs.  
639 13 and 14 are then contrasted with Figs. 11 and 12. The amount of residuals  
640 present in our model is comparable to the one present in the SIMAR database.  
641  $T_p$  shows a poorer fit (see Figs. 13c and 14c). The same poor fit is present in  
642 Figs. 11c and 12c. This behaviour can be explained because the wave-model  
643 (WAM and WAVEWATCH) considers *a priori* a parametrized wave-spectra.  
644 Such spectra has a predefined shape that does not necessarily represent the real  
645 sea state (Pallarés et al., 2014; Alomar et al., 2014). The method of represent-  
646 ing the wave-contingency with the principal directions seems to be useful to  
647 represent the wave-contingency (see Fig 11g). Regarding the SIMAR model,  
648 wave-directions from node N5 seems to differ significantly from the records of  
649 the nearest buoy, which suggests sensitivity of the wave-direction registry to the  
650 location of the node. The predicted growth and decay suffer rotation from the  
651 perfect fit, in the Q-Q plot, that is, central values are better fit than extreme  
652 ones (see Figs. 13e, 13f, 14e and 14f). Nonetheless, this better fit of the central  
653 values is also present for the node N5 in the SIMAR model ( see Figs. 11e and  
654 11f). Ergo, the SIMAR  $E$ ,  $E_{u,p}$ ,  $T_p$ ,  $D$  and  $\theta_p^*$  are well validated by the buoy  
655 datasets (see Figs. 11 and Fig. 12).

656 Storms simulated from the statistical model developed herein have been  
657 classified according to  $T_r$  (eq. 17), and represented in a series of pie-charts  
658 along the coast. It can be observed, for example, that  $E$  for a  $T_r$  of 5years is  
659 mainly of the highest values at nodes N1 through N4 (except at Roses Bay, N3),  
660 whereas the more southern coastal tracts present less  $E$  (see Fig. 15). Similar  
661 gradation occurs to  $D$  (see Fig. 15d), whereas a milder one occurs to  $H_{max}^*$  (see  
662 Fig. 15b) and none is observed in  $T_p$  (see Fig. 15c). In general, the same spatial  
663 gradations are observed at each respective storm component for any one of the

664  $T_r$  from 1 to 25 years.

## 665 6. Discussion

666 The discussion section will be divided into two parts: the first one will discuss  
667 the results from the proposed methodology (Model Building and Validation, in  
668 Fig. 2), whereas the second one will focus on the Wave-storm-generator.

### 669 6.1. The statistical model

670 This paper has proposed a statistical model that feeds upon a dataset from  
671 a wave-model (Section 3) which reproduces the main processes within the study  
672 area (Lionello, 2012). The Mediterranean Sea is characterized by local con-  
673 straints, such as mountain chains that funnel wind fluxes in a manner that  
674 limits the storm-pattern modes (Sánchez-Arcilla et al., 2008b). The Balearic Is-  
675 lands also trigger wave transformation-processes. At the south-most part of the  
676 central sector, the beach shoreline orientation induces a sheltering effect from  
677 northerly and easterly waves. It can be seen from Fig. 5 that the north-most  
678 part of the central sector is not sheltered from wave-storms. Strong forcings from  
679 the north and east directions cause the wind to exchange bursts of momentum  
680 with waves. The north direction has shorter fetch, while the east direction has  
681 different fetches depending on the location of the cyclo-genesis.

682 In a further consideration, the role of the sea level within a storm, especially  
683 when dealing with its consequences, is undeniable. Some authors (Masina et al.,  
684 2015) detected a considerable positive correlation between the peak water level  
685 (PWL) and the  $H_s$ . However, other authors (Mendoza et al., 2011) support the  
686 premise that the sea water level is independent from the storm conditions. This  
687 paper is based on the definition of storm-waves, therefore, it has focused only  
688 on storm-wave components, neglecting the effects of the water level.

689 The perception threshold in the Catalan Sea is  $H_s = 2.0\text{m}$  ( $H_{m0} \approx 2.1\text{m}$ )  
690 (Bolaños and Sánchez-Arcilla, 2006; DGP, 1992) and is introduced as an initial  
691 value in the iteration. The goodness-of-fit of observations to exponential models  
692 yield residuals to be analyzed. In Figs. 6a and 6e, as the threshold is low,  
693 these residuals are large, meaning that the corresponding  $D^*$  does not belong  
694 to exponential distributions. When the threshold rises, as observed in Figs. 6c,  
695 6d, 6g, and 6h, the residuals are minimized.

696 Bernardara et al. (2014) discussed that a limitation to this rise in threshold is  
697 the statistical significance in number of events over the threshold. It is observed  
698 in Figs. 7a and 7b that it is not recommended to go further than  $H_{m0} =$   
699  $3\text{m}$ . Model validation has served to refine the value to  $H_{m0} = 2.2\text{m}$ . This  
700 result intends to complement Sánchez-Arcilla et al. (2008a), which proposed  
701  $H_s = 2.0\text{m}$  based on mean-excess plots and Kolmogorov-Smirnov goodness-of-  
702 fit tests. The threshold  $H_{m0} = 2.2\text{m}$  is adequate because a) the associated  
703  $D^*$  is close to be exponentially distributed, b) the threshold falls in the linear  
704 part of the mean-excess-graphs, and c) the resulting storms are statistically  
705 significant in number. Please note that the fit to the exponential distribution is

706 not perfect, so the excess-over-threshold plot has been crucial in the selection of  
707 the storm-threshold.

708 On the other hand, the sensitivity test on  $D^*$  has shown that 12hrs is the  
709 most adequate value, since 48 or 72hrs lead to unrealistic storms that differ from  
710 field observations. Once storms are defined, it can be perceived that, in general,  
711 the northern Catalan coast is stormier than the southern one (see Table 2). N3  
712 behaves differently as it is located inside the Creus Cape (see Fig. 5), which  
713 shelters the area from cyclonic activity.

714 The validation of our model by the buoy records helps identify the sources  
715 of residuals in our model. For instance, the lesser similarity of  $T_p$  in our model  
716 to the buoy recorded  $T_p$  partly comes due to the difficulties of modelling this  
717 parameter with state-of-the art wave-models (WISE Group, 2007; Pallarés et al.,  
718 2014). Another possible explanation is that, for a given  $H_{m0}$ , the  $T_p$  depends  
719 heavily on fetch length and its origin. However, the influence of the  $T_p$  is not  
720 filtered by the intensity threshold.

721 Residuals in the growth-decay rates come from two main sources: physical  
722 and numerical. A physical source of residuals appears as offshore and onshore  
723 winds show distinct growth-decay rates, depending on remarkable differences in  
724 fetch extension. These differences can be compensated by uneven wind intensi-  
725 ties, but their effect remains in the growth and decay rates.

726 The numerical residuals in the growth-decay rates come from the third-grade  
727 polynomial, used to link growth-decay rates to  $D$ , and from the SIMAR dataset.  
728 The limitations of SIMAR datasets in representing growth-decay rates might be  
729 due to the fact that wave-models usually introduce residuals when reproducing  
730 sharp gradients (Cavaleri, 2009; Sánchez-Arcilla et al., 2014). This limitation  
731 may be partly alleviated with the novel terms for the wave-action-balance equa-  
732 tion (Zieger et al., 2015), that show better agreement with recent measurements.  
733 Also, at the study area, storm-wave patterns can be affected by current intensi-  
734 fications originated in the joint action of sustained winds from the NE-SE plus  
735 a shelf narrowing effect (Mestres et al., 2016). Thus, coupling the wave-model  
736 with a high resolution circulation model may improve the results. The short-  
737 coming of the third-degree polynomial is that it has difficulties reflecting a link  
738 of the growth-decay rates for a  $D$  below 100hrs, where a dense cloud of values is  
739 present (see Fig. 10); further research on the intra-time distribution module is  
740 on-going. Apart from these issues, the statistical model reproduces the promi-  
741 nent features at the study area, and the storm components show agreement with  
742 the buoy records.

743 It can be inferred from the HAC results (see table 4) that the strongest de-  
744 pendent variables are  $\log D$  and  $\log E$ . This dependency structure is consistent  
745 with physical observations, as the most enduring storms are usually those which  
746 have higher hydrodynamic forcings. It can be argued that, as  $E$  is integrated  
747 over  $D$ , that the correlation between them has to be the most prominent. The  
748 outcomes also show that, despite some dependence exists between  $E_{u,p}$  and the  
749  $E$  or the  $D$ , the dependence among  $E_{u,p}$  and  $(E, D)$  is weaker. This behaviour  
750 can be explained due to the point-based definition of  $E_{u,p}$  that presents more  
751 variability than the integrated values of  $E$  and  $D$ , that features lower variabil-

752 ity. It can be observed how  $\tau_{(E,D)}$  increases northward (Fig. 8), implying more  
753 correlation between durations and northern storm magnitudes. At nodes where  
754 type A trees are prevalent, not only  $E$ , but also  $H_{max}^*$  is co-dependent on  $D$ .

755 Please regard that  $\theta_p^*$  is the direction of the storm-peak, and therefore repre-  
756 sents the storm at its peak, rather than being a mean direction of the event. The  
757 East is one of the principal  $\theta_p^*$ , and the main effective  $\theta_p^*$  at a great part of the  
758 Catalan coast. Waves that blow northward from the Gulf of Lyon tend to veer  
759 counter-clockwise and do not impact at the Catalan coast (Bolaños et al., 2009).  
760 The coastline orientation (from N6 northward) is the reason, as despite having  
761 more recorded storms at the SIMAR points, the effective storms obtained with  
762 synthetic simulations were not as significant in number than the other southern  
763 points. Due to larger fetch, from N6 northward, northern  $\theta_p^*$  are dominating.  
764 From N7 southward, the southern waves gain importance. The buoy used to  
765 validate either SIMAR or our data should be as close as possible to the node in  
766 the model to validate, as  $\theta_p^*$  is considerably sensible to location.

767 The intercept of the growth-rate is, generally, 0.46, as well as the intercept  
768 of the decay-rate (see table 7). Both growth and decay-rates are considerably  
769 independent of  $D$  for durations under 100hrs. However, for  $D > 100$ hrs, while  
770 the growth-rate become asymptotic to 0.8, the decay-rate becomes asymptotic to  
771 0.2. That is, under this condition of  $D$ , more durable storms tend to also present  
772 higher growth-rates and lower decay-rates. Such large growth-rate and small  
773 decay-rate contradict the common phenomenon. The high  $T_r$  events recorded  
774 at the Catalan coast (November 2001, October 2003 and December 2008) are  
775 scarce, but reflect this sharp gradient response, veered by the pulsative wind  
776 momentum.

777 The eq. 17 and 18, of  $T_r$ , by being arithmetic and geometric averages,  
778 respectively, set physical constraints on each marginal variable. This equalizes  
779 the marginal  $T_r$  of each variable to the total  $T_r$  of the storm, as real maritime  
780 storms present such equivalence between marginal and total  $T_r$ . For example,  
781 when the  $T_r$  of a storm is 10yrs, the storm should not have a  $H_{m0}$  of  $T_r = 50$ yrs  
782 and a  $D$  of  $T_r = 1$ yrs. The  $T_r$  from eq. 17, in particular, provides the best  
783 constraints to the  $T_r$  of each integrating marginal storm component.

784  $E$  and  $D$  can reach significantly large values with increasing  $T_r$  at the North  
785 (see Figs. 15a and 15d). Eastern storms generated at the Ligurian Sea are the  
786 most energetic and lasting storms due to the fetch distance (near 600 km). For  
787  $T_r = 5$ yrs (see Fig. ?? and the section below), larger  $D$  can significantly affect  
788  $E$ , as  $H_{m0}$  appears to be more spatially uniform along the Catalan coast.

## 789 6.2. Application

790 In order to visualize the potential of the methodology used, an example of  
791 the characterization of storms for a  $T_r = 5$ years is presented. The 5-year  $T_r$  has  
792 been selected because it is an extreme condition in which a) SIMAR dataset  
793 has a representative number of samples and b) the order of magnitude of such  
794 category has been analysed in detail for the study area (Mendoza et al., 2011;  
795 Sánchez-Arcilla et al., 2008b). As to provide suitable data for elements on the  
796 coast, the land originated storms (non-effective storms) are filtered from the set

797 of synthetic storms. Note that, as the principal directions at some nodes might  
 798 be land-generated, the number of effective storms decrease considerably after  
 799 the filtering, compared to other nodes.

800 Our model provides joint combinations of  $E$ ,  $E_{u,p}$ ,  $T_p$ ,  $D$ ,  $\theta_p^*$  and growth-  
 801 decay rates. The outcomes of the model can be examined at Fig. 15. The  
 802 seven predicted variables are summarized in pie-charts, the categories of which  
 803 describe the differences and principal patterns that appear on a particular node.  
 804 One of the main findings of this paper is that, rather than a single value that  
 805 represents a particular category (i.e. a  $T_r$ ) for a specific wave component, a  
 806 range of plausible values can be considered, instead. Note, however, that within  
 807 this plausible range, there may be various intervals of disparate frequency (i.e.  
 808 particular intervals shown in the pie-charts). The seven variables are linked via  
 809 statistical models and it appears that a wide range of possibilities satisfy the  
 810 clustering criteria. A description of the general study area is provided, whereas  
 811 numeric outcomes are given for an example-node, N5.

812 The Storm-intensity sub-model provides the first variables of the synthetic  
 813 storms generated by our model. Fig. 15b shows that the  $H_{max}^*$  can range from  
 814 2.2m (by definition) to over 8m. The highest waves are located in the northern  
 815 coast-sector, and decreases southward, just as described in Sec. 5. mode( $H_{max}^*$ )  
 816 at node N5 is (6, 7.5] m (mode( $H_{1/3}$ ) = (5.7, 7.1] m). Fig. 15c shows that  $T_p$   
 817 is independent from the location along the coast. The mode( $T_p$ ) at node N5  
 818 is (11, 12.5] s.  $D$  presents a clear boundary at node C2: southward of node C2,  
 819 storms generally span 48hrs (2days) of duration (see Fig. 15d). The mode( $D$ )  
 820 is > 96hr. Fig. 15a shows a geographical distribution that is clearly the result  
 821 of a combination of the effects of both  $H_{m0}$  and  $D$ . The mode( $E$ ) at node N5  
 822 is > 2000m<sup>2</sup> hr. The above-mentioned large values for mode( $D$ ) and mode( $E$ )  
 823 are due to the effects of the GPD extreme value functions and the Gumbel  
 824 HAC, and they surpass physical constraints to such storm components, so the  
 825 values of 96hrs and 2000m<sup>2</sup> hr are to be used for mean- $D$  ( $\bar{D}$ ) and mean- $E$  ( $\bar{E}$ ),  
 826 respectively. These values reinforce the existing idea that storms magnitudes at  
 827 the northern part of the coast are higher than at the rest of the coast.

828 The Directionality sub-model specifies that the  $\theta_p^*$  along the Catalan coast  
 829 are mainly eastern directions (see Fig. 15e). At node N5, in particular, the  
 830 principal peak-wave direction is 76.27° (see Table 5); this is the PC2 at node  
 831 N5, but regard that PC1 is not an effective wave-direction.

832 The Intra-time distribution sub-model reproduce higher growth-rates than  
 833 decay ones (see Figs. 15f and 15g). The exception is at the Northern nodes,  
 834 where longer fetches exist and thus, a wider variety of wave ages can be found.  
 835 The growth-decay rates are geographically uniform, although this is due to an  
 836 above-mentioned limitation of the SIMAR model and the Intra-time distribution  
 837 sub-model. The growth-rate to consider at node N5 is (0.5, 0.6], and the decay-  
 838 rate is (0.3, 0.4].

839 The results from our model are compared to the conventional engineering  
 840 approach, where, given a  $T_r$  and a location, a  $H_s$  is obtained, followed by the  
 841  $T_p$ . The conventional method presents the following 90% confidence interval,  
 842 for  $T_r = 5$  yrs,  $H_s = (4.3, 5) m$ , and  $T_p = (12.4, 12.8) s$  (CIIRC, 2010). The

843  $D$  is usually considered as 24hrs in the Catalan Sea. The storm wave-height  
 844 evolution is usually modelled by an isosceles triangle where the height is the  
 845 maximum  $H_s$ . In this case, the conventional  $\bar{E}$  is  $(491.7, 726) m^2 h$ , and other  
 846 information such as incoming wave-direction can be obtained from contingency  
 847 tables in the literature.

848 The storms from our model are consistent with the values provided in Men-  
 849 doza et al. (2011); Sánchez-Arcilla et al. (2008b). The  $H_s$  and the  $T_p$  in our  
 850 model are slightly larger than in the conventional methodology, in this case,  
 851 without significant physical implications.  $\bar{E}$  and  $\bar{D}$  from our model, although  
 852 considerably larger, are possibly more accurate than their classical counterparts,  
 853 and the same applies to the growth-decay rates. Also,  $D = 24$ hrs is an average  
 854 duration, while  $D = (114, 168]$  hrs derives from the SIMAR dataset.  $\theta_p^*$  is an  
 855 extra information provided here and which is not so much considered in the  
 856 conventional approach. Most importantly, the conventional methodology can  
 857 hardly reflect the probable behaviour of the storm, mainly because it ignores  
 858 the variable interactions and feedbacks.

## 859 7. Conclusions

860 The statistical wave-storm model proposed is composed by three sub-modules:  
 861 a) Storm-intensity, b) Wave-directionality and c) Intra-time distribution. In  
 862 these sub-modules, waves have been defined by a set of storm-components ( $E$ ,  
 863  $E_{u,p}$ ,  $T_p$ ,  $D$ ,  $\theta_p^*$  and growth-decay rates), representing their nature in a more  
 864 accurate manner. Our model is well validated by buoy records, whereas main  
 865 sources of residuals are related to growth-decay rates.

866 Storms have been defined with a threshold of  $H_{m0} = 2.2$ m, which has been  
 867 obtained after testing on  $D^*$ , plus  $H_{m0}$  excess-over-threshold plots.

868 In the Intensity sub-model, the marginal distributions of each variable are  
 869 characterized by GPDs, whereas dependences among the variables are repre-  
 870 sented by HACs. The best fitting HAC type is Gumbel. It is observed that  
 871 the strongest dependence may be between  $E$  and  $D$ . Two HAC structures are  
 872 observed along the Catalan coast: type A and type B, depending on the degree  
 873 of semi-dependence between  $E_{u,p}$  and  $(E, D)$ . The semi-dependence param-  
 874 eter  $\tau_{(E,D)}$  increases northward. Therefore, northern  $E$  and  $D$  present more  
 875 correlation.

876 Wave-directions are described via movM. The movM distribution is selected  
 877 using a statistic from the Watson test as convergence criteria. The princi-  
 878 pal peak-wave incoming-direction,  $\theta_p^*$ , at N1 to N6 are, by decreasing order  
 879 of importance, North and East; whereas eastern and southern directions are  
 880 predominant from N7 to S7.

881 The most appropriate model for wave-height evolution is the irregular-trapezoidal  
 882 model. On the other hand, the growth-decay rates are related to the rest of the  
 883 storm components through a polynomial relationship with  $D$ . A mean behaviour  
 884 of  $D$  for  $D < 100$ hrs is reproduced by the model, although for greater  $D$  the  
 885 model tends to predict higher growth rates and lower decay rates.

886 One feature of our model is its ability to generate synthetic storm conditions  
887 and to classify them by  $T_r$ ; these storms are evaluated in the form of pie-charts.  
888 In general, for a  $T_r$  of 5yrs, storms at the northern Catalan coast have greater  
889  $E$ ,  $D$ , and  $H_{m0}$ ; while  $T_p$  are similar to central or southern Catalan coasts.  
890 Also, the principal  $\theta_p^*$  is eastern and the growth and decay rates approximate  
891 0.55 and 0.35, respectively.

## 892 8. Acknowledgements

893 This article has been supported by the EU-projects iCOAST (Grant Agree-  
894 ment 661ECHO/SUB/2013/009) and RISES-AM (FP7-ENV-693396), and the  
895 Spanish national project PLAN-WAVE (CTM2013-45141-R). As a group, we  
896 would like to thank the Secretary of Universities and Research of the depart-  
897 ment of Economics of the Catalan Generalitat (Ref. 2014SGR1253). The second  
898 author acknowledges the PhD scholarship from the Government of Catalonia  
899 (DGR FI-AGAUR-14). The support of the Puertos del Estado and XIOM buoy  
900 network is duly appreciated. The authors would also like to thank Prof. Dr.  
901 Ostap Okhrin and Mr. Alexander Ristig for their invaluable guidance on the  
902 use of the HAC R package; to Dr. Maribel Ortego and Prof. Dr. Juan Jose  
903 Egozcue, for their comments on the statistical aspects of the work; Dr. Bettina  
904 Grün, Prof. Peter Jupp and Prof. Alan Gelfand for their patient guidance on  
905 directional statistics. Special thanks are also acknowledged to two anonymous  
906 peer-reviewers whose genuinely constructive comments have enriched this paper.

## 907 9. References

- 908 Alomar, M.: 2012, ‘Improving wave forecasting in variable wind conditions.  
909 The effect of resolution and growth rate for the Catalan coast’. Ph.D. thesis,  
910 Barcelona-Tech.
- 911 Alomar, M., A. Sánchez-Arcilla, R. Bolaños, and A. Sairouni: 2014, ‘Wave  
912 growth and forecasting in variable, semi-enclosed domains’. *Continental Shelf  
913 Research* **87**, 28–40.
- 914 Barnerjee, A., I. Dhillon, J. Ghosh, and S. Sra: 2005, ‘Clustering on the Unit Hy-  
915 persphere using von Mises-Fisher Distributions’. *Journal of Machine Learning  
916 Research* **6**, 1345–1382.
- 917 Bernardara, P., F. Mazas, X. Kergadallan, and L. Hamm: 2014, ‘A two-step  
918 framework for over-threshold modelling of environmental extremes’. *Natural  
919 Hazards and Earth System Sciences* **14**, 635–647.
- 920 Bolaños, R.: 2004, ‘Tormentas de oleaje en el Mediterraneo: Física y predicción’.  
921 Ph.D. thesis, BarcelonaTech.
- 922 Bolaños, R., G. Jordà, J. Cateura, J. López, J. Puigdefàbregas, J. Gómez, and  
923 M. Espino: 2009, ‘The XIOM: 20 years of a regional coastal observatory in  
924 the Spanish Catalan coast’. *Journal of Marine Systems* **77**, 237–260.

- 925 Bolaños, R. and A. Sánchez-Arcilla: 2006, ‘A note on nearshore wave features:  
926 implications for wave generation’. *Progress in Oceanography* **70**, 168–180.
- 927 Cavaleri, L.: 2009, ‘Wave Modeling - Missing the Peaks’. *Journal of Physical*  
928 *Oceanography* **39**(2757-2778).
- 929 Chen, X., Y. Fan, and A. Patton: 2004, ‘Simple tests for models of dependence  
930 between multiple financial time series, with applications to US equity returns  
931 and exchange rates’. *London Economics Financial Markets Group Working*  
932 *Paper* –(483).
- 933 Cherubini, U., E. Luciano, and W. Vecchiato: 2004, *Copula methods in finance*.  
934 John Wiley & Sons Ltd.
- 935 CIIRC: 2010, ‘State of the Catalan coastline’. Technical report, CIIRC.
- 936 Coles, S.: 2001, *An introduction to Statistical modeling of extreme values*.  
937 Springer.
- 938 Corbella, S. and D. Stretch: 2012, ‘Multivariate return periods of sea storms for  
939 coastal erosion risk assessment’. *Natural Hazards and Earth System Sciences*  
940 **12**, 2699–2708.
- 941 Corbella, S. and D. D. Stretch: 2013, ‘Simulating a multivariate sea storm using  
942 Archimedean copulas’. *Coastal Engineering* **76**, 68–78.
- 943 De Michele, C. and G. Salvadori: 2003, ‘A Generalized Pareto intensity-duration  
944 model of storm rainfall exploiting 2-Copulas’. *Journal of Geophysical Research*  
945 **108**(D2), 4067.
- 946 de Waal, D. J. and P. H. A. J. M. van Gelder: 2005, ‘Modelling of extreme wave  
947 heights and periods through copulas’. *Extremes* **8**, 345–356.
- 948 DGP: 1992, ‘ROM 0.3-91 Recommendations for waves and atlas of maritime  
949 climate on Spanish coast’. Direccion General de Puertos.
- 950 DGP: 2001, ‘ROM 0.0 General procedures and computations basics. On mar-  
951 itime and harbour projects. Part I’. Direccion General de Puertos.
- 952 Eastoe, E., S. Koukoulas, and P. Jonathan: 2013, ‘Statistical measures of ex-  
953 tremal dependence illustrated using measured sea surface elevations from a  
954 neighbourhood of coastal locations’. *Ocean Engineering* **62**, 68–77.
- 955 Embrechts, P., C. Klüppelberg, and T. Mikosch: 1997, *Modelling extremal*  
956 *events, volume 33 of Applications of Mathematics*. New York. Springer-Verlag,  
957 Berlin.
- 958 Gan, F., K. Koehler, and J. Thompson: 1991, ‘Probability Plots and Distri-  
959 bution Curves for Assessing the Fit of Probability Models’. *The American*  
960 *Statistician* **45**(1), 14–21.



- 961 García-León, M., V. Gràcia, L. Robichaux, A. Kroger, J. Gault, and A. Sánchez-  
962 Arcilla: 2015, *Evaluation of transient defence measures against storms*,  
963 Chapt. 166. World Scientific.
- 964 Genest, C. and A.-C. Favre: 2007, ‘Everything you always wanted to know about  
965 copula modeling but were afraid to ask’. *Journal of hydrologic engineering*  
966 **12**(4), 347–368.
- 967 Genest, C. and B. Remillard: 2004, ‘Test of independence and randomness based  
968 on the empirical copula process’. *Test* **13**, 335–369.
- 969 Goda, Y.: 2010, *Random Seas and Design of Maritime Structures*, Vol. 33.  
970 World Scientific, 3rd edition.
- 971 Gomez, M. and J. Carretero: 2005, ‘Wave forecasting at the Spanish coasts’.  
972 *Journal of Atmospheric and Ocean Science* **10**(4), 389–405.
- 973 Gràcia, V., M. García, M. Grifoll, and A. Sánchez-Arcilla: 2013, ‘Breaching  
974 of a barrier under extreme events. The role of morphodynamic simulations’.  
975 *Journal of Coastal Research* **65**, 951–956.
- 976 Grifoll, M., A. Aretxabaleta, and M. Espino: 2015, ‘Shelf response to intense  
977 offshore wind’. *Journal of Geophysical Research: Oceans* **120**(9), 6564–6580.
- 978 Hofert, M. and M. Machler: 2011, ‘Nested Archimedean Copulas Meet R—The  
979 nacopula Package’. *Journal of Statistical Software*.
- 980 Holthuijsen, L.: 2007, *Waves in oceanic and coastal waters*. Cambridge Univer-  
981 sity Press.
- 982 Hosmer, D., S. Lemeshow, and R. Sturdivant: 2013, *Applied Logistic Regression*,  
983 *3rd Edition*. Wiley. 528 pp.
- 984 Kendall, M.: 1937, ‘A new measure of rank correlation’. *Biometrika* **6**, 83–93.
- 985 Li, F., P. van Gelder, R. Ranasinghe, D. Callaghan, and R. Jongejan: 2014,  
986 ‘Probability modelling of extreme storms along the Dutch coast’. *Coastal*  
987 *Engineering* **86**, 1–13.
- 988 Lionello, P. (ed.): 2012, *The climate of the Mediterranean region*. Elsevier.
- 989 Mardia, K. and P. Jupp: 2009, *Directional statistics*, Vol. 494. John Wiley &  
990 Sons.
- 991 Martin-Soldevilla, M., M. Martin-Hidalgo, V. Negro, J. Lopez-Gutierrez, and  
992 P. Aberturas: 2015, ‘Improvement of theoretical storm characterization for  
993 different climate conditions’. *Coastal Engineering* **96**, 71–80.
- 994 Masina, M., A. Lamberti, and R. Archetti: 2015, ‘Coastal flooding: A copula  
995 based approach for estimating the joint probability of water levels and waves’.  
996 *Coastal Engineering* **97**, 37 – 52.

- 997 Mazas, F., X. Kergadallan, P. Garat, and L. Hamm: 2014, ‘Applying POT  
998 methods to the revised joint probability method for determining extreme sea  
999 levels’. *Coastal Engineering* **91**, 140–150.
- 1000 Melby, J. and N. Kobayashi: 2011, ‘Stone armor damage initiation and pro-  
1001 gression based on the maximum wave momentum flux’. *Journal of Coastal*  
1002 *Research* **27**, 110–119.
- 1003 Mendoza, E. T., J. Jimenez, and J. Mateo: 2011, ‘A coastal storms intensity  
1004 scale for the Catalan sea (NW Mediterranean)’. *Natural Hazards and Earth*  
1005 *System Science* **11**(9), 2453–2462.
- 1006 Mestres, M., M. Grifoll, and A. Sánchez-Arcilla: 2016, ‘Analysis of current inten-  
1007 sification in the Northwest Mediterranean shelf’. *Continental Shelf Research*  
1008 **114**, 29 – 40.
- 1009 Okhrin, O., Y. Okhrin, and W. Schmid: 2013, ‘On the structure and estimation  
1010 of hierarchical Archimedean copulas’. *Journal of Econometrics* **173**, 189–204.
- 1011 Okhrin, O. and A. Ristig: 2012, ‘Hierarchical Archimedean copulae: the HAC  
1012 package’. Humboldt-Universität zu Berlin.
- 1013 Ortego, M., R. Tolosana-Delgado, J. Gibergans-Báguena, J. Egozcue, and A.  
1014 Sánchez-Arcilla: 2012, ‘Assessing waviestorm hazard evolution in the NW  
1015 Mediterranean with hindcast and buoy data’. *Climatic Change* **113**, 713–  
1016 731.
- 1017 Pallarés, E., A. Sánchez-Arcilla, and M. Espino: 2014, ‘Wave energy balance in  
1018 wave models (SWAN) for semi-enclosed domains—application to the Catalan  
1019 coast’. *Continental Shelf Research* **87**, 41–53.
- 1020 Pewsey, A., M. Neuhäuser, and G. Ruxton: 2013, *Circular statistics in R*. Ox-  
1021 ford University Press.
- 1022 Salvadori, G. and C. De Michele: 2004, ‘Frequency analysis via copulas: The-  
1023 oretical aspects and applications to hydrological events’. *Water Resources*  
1024 *Research* **40**(12), W12511.
- 1025 Salvadori, G. and C. De Michele: 2010, ‘Multivariate multiparameter extreme  
1026 value models and return periods: A copula approach’. *Water Resources Re-*  
1027 *search* **46**.
- 1028 Salvadori, G., C. De Michele, N. Kottegoda, and R. Rosso: 2007, *Extremes in*  
1029 *nature: An approach using copulas*. Springer.
- 1030 Salvadori, G., G. Tomicchi, and F. d’Alessandro: 2014, ‘Practical guidelines  
1031 for multivariate analysis and design in coastal and off-shore engineering’.  
1032 *Coastal Engineering* **88**, 1–14.

- 1033 Sánchez-Arcilla, A., J. G. Aguar, J. Egozcue, M. Ortego, P. Galiatsatou, and P.  
1034 Prinos: 2008a, ‘Extremes from scarce data: The role of Bayesian and scaling  
1035 techniques in reducing uncertainty’. *Journal of Hydraulic Research* **46**(sup2),  
1036 224–234.
- 1037 Sánchez-Arcilla, A., M. García, and V. Gràcia: 2014, ‘Hydro-morphodynamic  
1038 modelling in Mediterranean storms - errors and uncertainties under sharp  
1039 gradients’. *Nat. Hazards Earth Syst. Sci.* **14**, 2993–3004.
- 1040 Sánchez-Arcilla, A., M. García-León, V. Gràcia, R. Devoy, A. Stanica, and  
1041 J. Gault: (in press), ‘Managing coastal environments under climate change:  
1042 pathways to adaptation’. *Science of the Total Environment*.
- 1043 Sánchez-Arcilla, A., D. González-Marco, and R. Bolaños: 2008b, ‘A review of  
1044 wave climate and prediction along the Spanish Mediterranean coast’. *Nat.*  
1045 *Hazard. Earth Sys.* **8**(6), 1217–1228.
- 1046 Sklar, A.: 1959, *Fonctions de répartition à n dimension et leurs marges*. Uni-  
1047 versité Paris 8.
- 1048 Tolman, H.: 2009, ‘User manual and system documentation of WAVEWATCH  
1049 III version 3.14.’. Technical report, NOAA / NWS / NCEP / MMAB.
- 1050 Tolosana-Delgado, R., M. Ortego, J. Egozcue, and A. Sánchez-Arcilla: 2010,  
1051 ‘Climate change in a Point-over-threshold model: an example on ocean-wave-  
1052 storm hazard in NE Spain’. *Advances in Geosciences* **26**, 113–117.
- 1053 Tolosana-Delgado, R., M. Ortego, J. Egozcue, and A. Sánchez-Arcilla: 2011,  
1054 ‘Checking model-data weather hazard occurrence fit in the context of climate  
1055 change’. In: *Proceedings of the 2011 Annual Conference of the International*  
1056 *Association for Mathematical Geosciences*. pp. 870–877.
- 1057 Trivedi, P. and D. Zimmer: 2007, *Copula modeling: an introduction for practi-*  
1058 *tioners*. Now Publishers Inc.
- 1059 Unden, P., L. Rontu, H. Jarvinen, P. Lynch, J. Calvo, G. Cats, J. Cuixart, K.  
1060 Eerola, C. Fortelius, J. A. Garcia-Moya, C. Jones, G. Lenderlink, A. McDon-  
1061 ald, R. McGrath, B. Navascues, N. W. Nielsen, V. Odergaard, E. Rodrigues,  
1062 M. Rummukainen, R. Room, K. Shattler, B. H. S. nd H. Savijarvi, B. Schreur,  
1063 R. Sigg, H. The, and A. Tijn: 2002, ‘HIRLAM-5 Scientific Documentation’.  
1064 Technical report, HIRLAM-5 Project, c/o Per Unden SMHI, S-601 76 Nor-  
1065 rkoping, SWEDEN. 144 p.
- 1066 Wackernagel, H.: 2003, ‘Ordinary kriging’. In: *Multivariate Geostatistics*.  
1067 Springer Berlin Heidelberg, pp. 79–88.
- 1068 Wahl, T., J. Jensen, and C. Muddersbach: 2011, ‘A multivariate statistical model  
1069 for advanced storm surge analyses in the North Sea’. *Coastal Engineering*  
1070 *Proceedings* **1**(32), 19.

- 1071 Wahl, T., C. Mudersbach, and J. Jensen: 2012, ‘Assessing the hydrodynamic  
1072 boundary conditions for risk analyses in coastal areas: a multivariate statisti-  
1073 cal approach based on copula functions’. *Natural Hazards and Earth System  
1074 Science* **12**(2), 495–510.
- 1075 WAMDI Group, S. H., K. Hasselmann, P. A. E. M. Janssen, G. J. Komen, L.  
1076 Bertotti, P. Lionello, A. Guillaume, V. C. Cardone, J. A. Greenwood, M.  
1077 Reistad, L. Zambresky, and J. A. Ewing: 1988, ‘The WAM model: a third-  
1078 generation ocean wave prediction model’. *Journal of Physical Oceanography*  
1079 **18**, 1775–1810.
- 1080 WISE Group: 2007, ‘Wave modelling-the state of the art’. *Prog. Oceanogr.* **75**,  
1081 603–674.
- 1082 Wojtanowicz, A. M.: 2010, ‘Twin Storm Events: A probability analysis and risk  
1083 evaluation of twin storm occurrences along the coast of Catalonia’. Master’s  
1084 thesis, UPC Barcelona-Tech.
- 1085 Zieger, S., A. V. Babanin, W. E. Rogers, and I. R. Young: 2015, ‘Observation-  
1086 based source terms in the third-generation wave model {WAVEWATCH}’.  
1087 *Ocean Modelling* **96, Part 1**, 2 – 25. Waves and coastal, regional and global  
1088 processes.

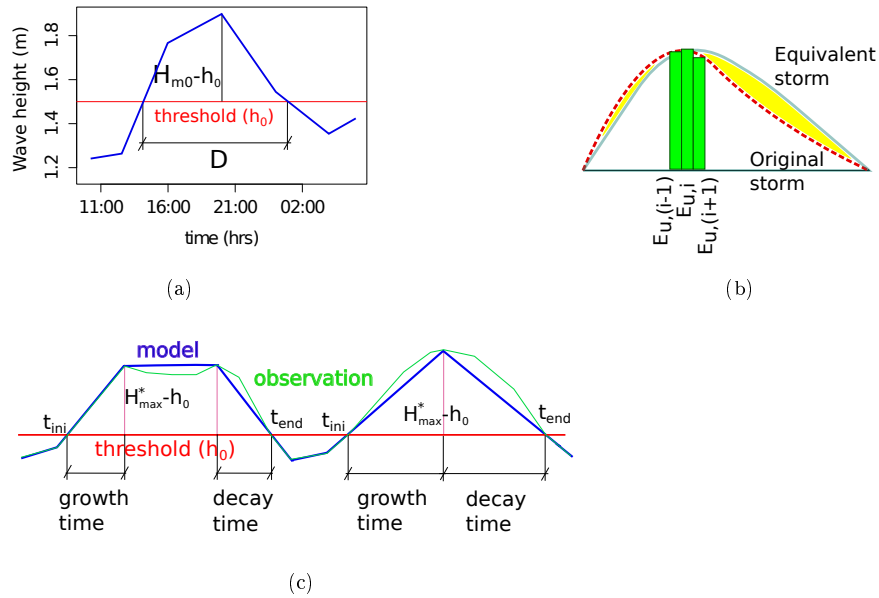


Figure 1: a) Definition of variables for a single peak storm, where  $H_{m0}$  is the wave-height,  $D$  is the storm duration, b) definition of the peak-unitary-storm energy,  $E_{u,p}$ , where  $E_{u,i}$  are the unitary-storm-energies at each hour (the red dashed line is the actual storm and the green line is an equivalent storm without the skewness problem), c) proposed storm shapes (irregular-trapezoid and triangular), where the parameters are initial time ( $t_{ini}$ ), ending time ( $t_{end}$ ), and our model's maximum wave-height ( $H_{max}^*$ ).

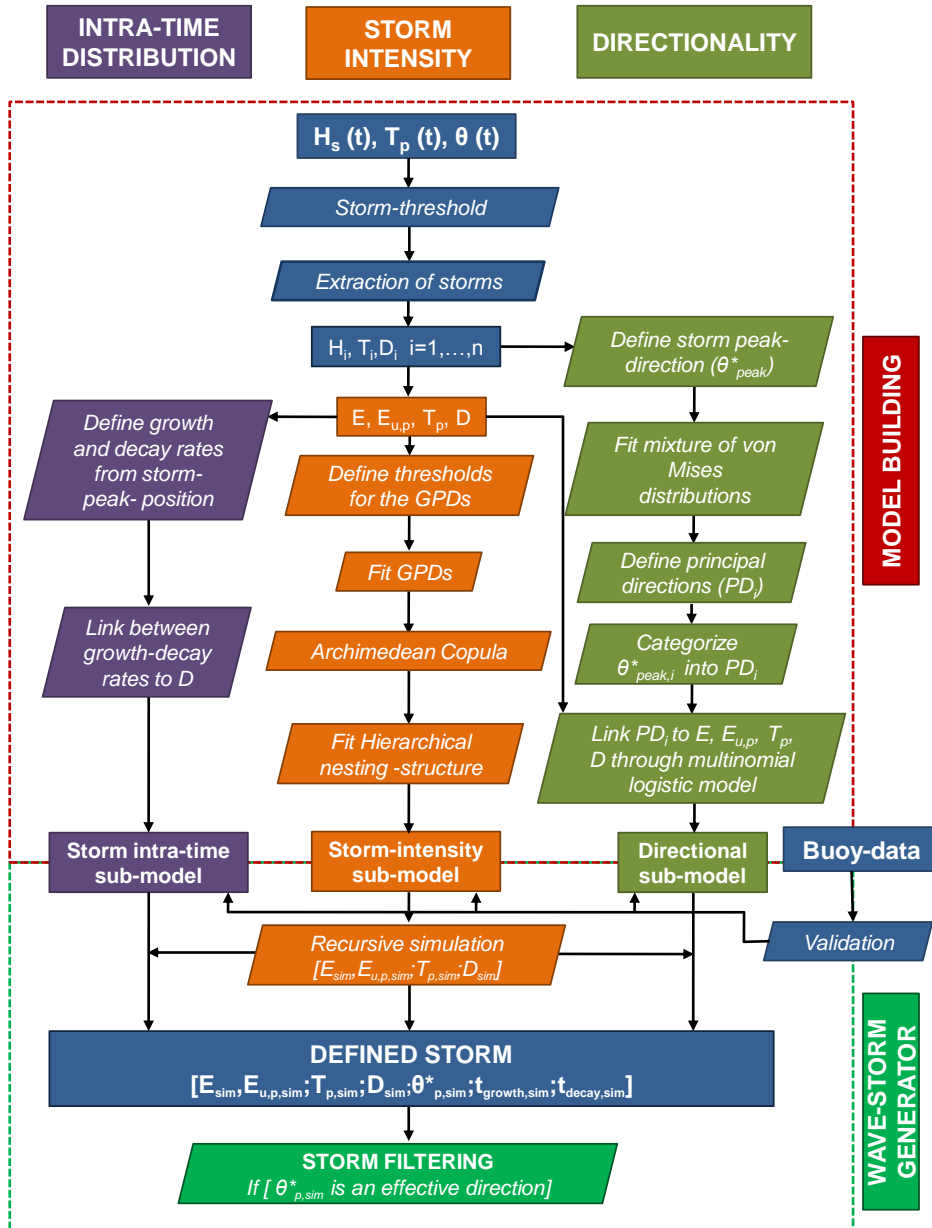


Figure 2: Flow-chart of the methodology used to construct the statistical storm model. The model is composed by three sub-models: intensity (orange), wave directionality (olive green) and intra-time (purple). Rectangle boxes represent input/output data whereas the parallelograms represent the actions taken.

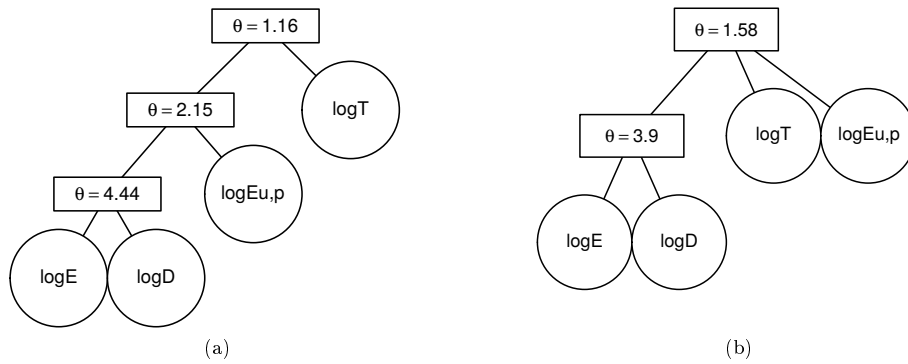


Figure 3: Types of HAC trees obtained for the Catalan Sea. a) Type-A: HAC structured with 3 levels of variable dependencies (at node N1), b) type-B: HAC structured with 2 levels of variable dependencies (at node N7). The upmost level is the «root». The variables sequentially cluster according to their dependence ( $\theta$ ) with other variables.

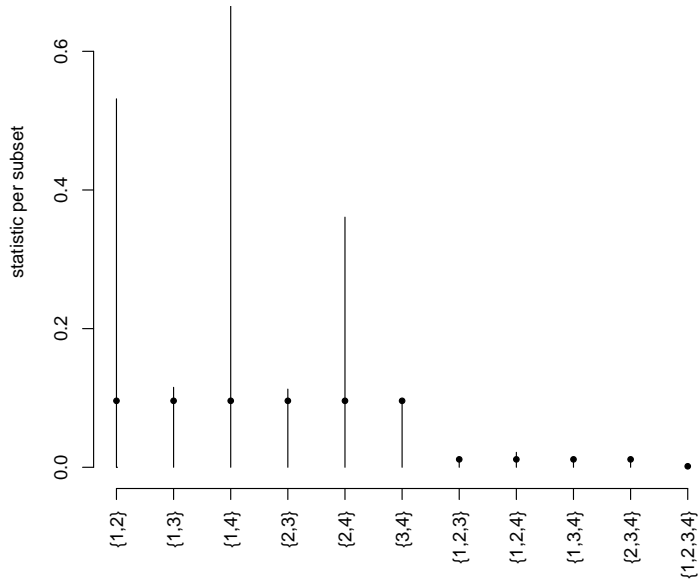


Figure 4: Dependogram: dependence among variables  $\log E$  (1),  $\log E_{u,p}$  (2),  $\log T$  (3), and  $\log D$  (4), at node C3. The length of the bar (statistic) exceeding the bullet (critical value) represents the degree of dependence.  $E$  and  $D$  present the greatest dependence, followed by the subsets  $\{E, E_{u,p}\}$  and  $\{E_{u,p}, D\}$ .



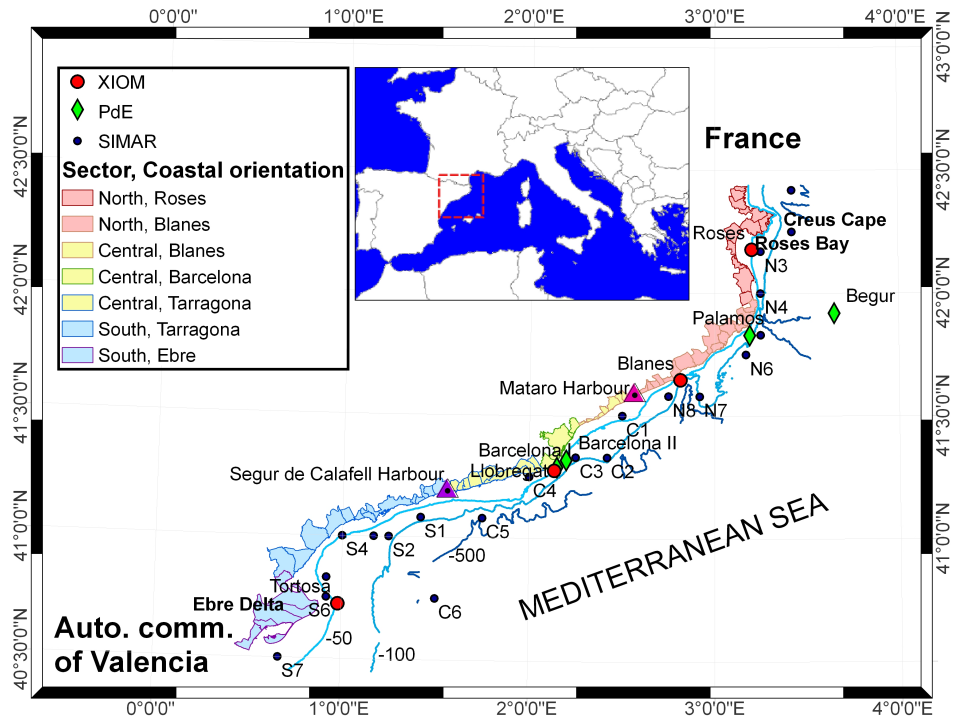


Figure 5: Map of the study area showing wave measurement networks (XIOM and PdE), and the SIMAR nodes. The colour lines of the regions (red, orange, green, blue and purple) and the coloured areas (red, yellow and blue) cluster the coast into the three sectors: North (France to Mataro harbour), Central (Mataro harbour to Segur de Calafell harbour) and South (Segur de Calafell harbour to the Autonomous Community of Valencia).

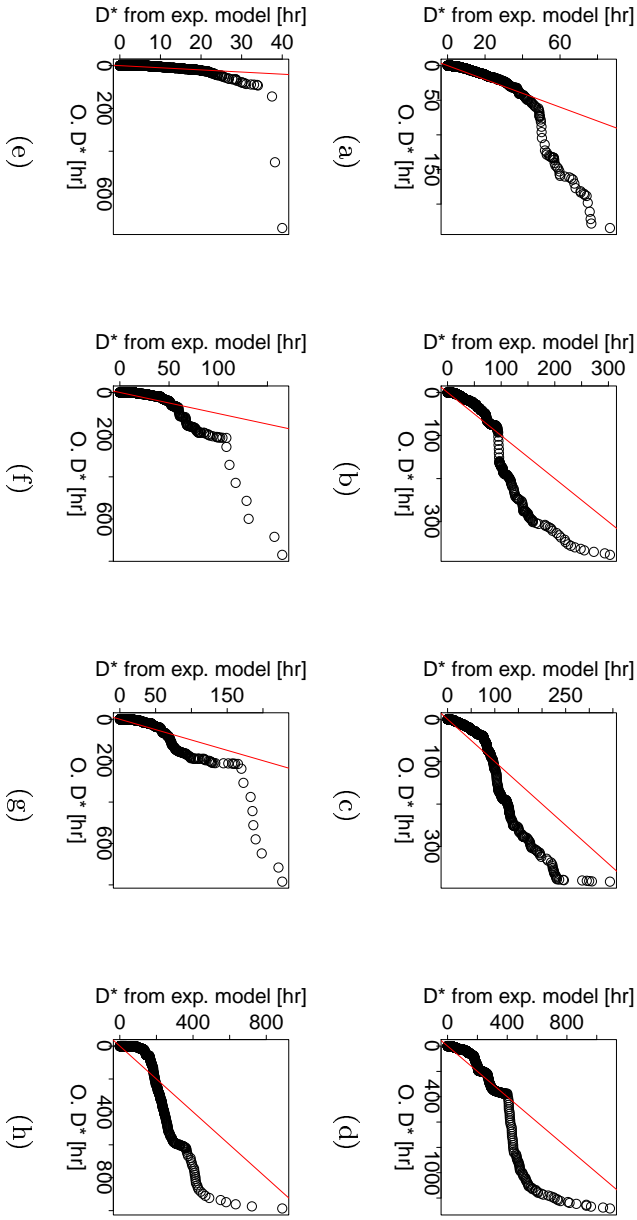


Figure 6: Q-Q plot of the observed  $D^*$  (x-axis) and  $D^*$  from the corresponding best-fit exponential model (y-axis). The red line represents null residuals (1:1 ratio), while the circles are the scatter points. From a) to d), the time lags are obtained using a storm-threshold of: 1.5m, 2.1m, 2.2m, and 3m, respectively, for G3 node. From e) to h), it is the same for the PdF-Barcelona-II buoy node.

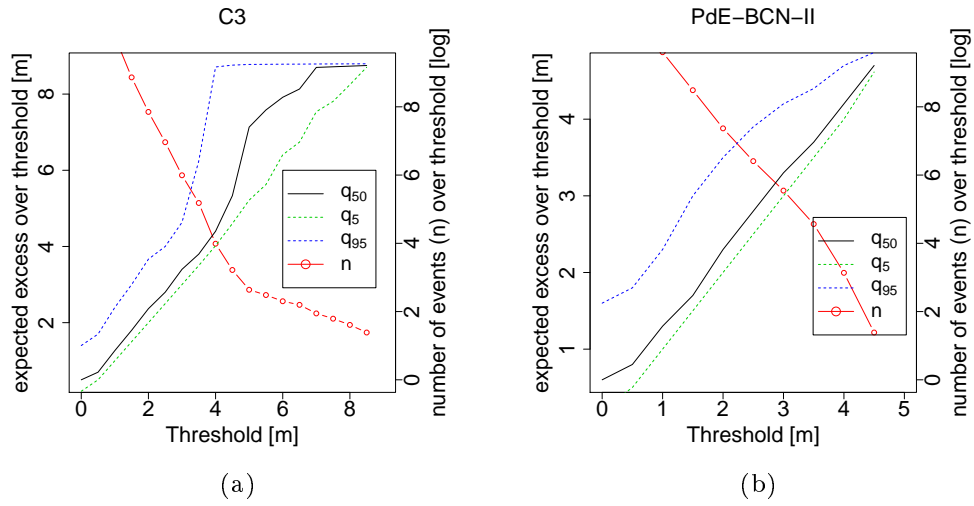


Figure 7: Mean-excess-plot of  $H_{m0}$  for the a) SIMAR node C3 and b) PdE-BCN-II buoy node. The red line represents the log-transformed number of events over a given threshold, while  $q_{50}$ ,  $q_5$  and  $q_{95}$  are the quantiles 50, 5 and 95, of  $H_{m0}$ .

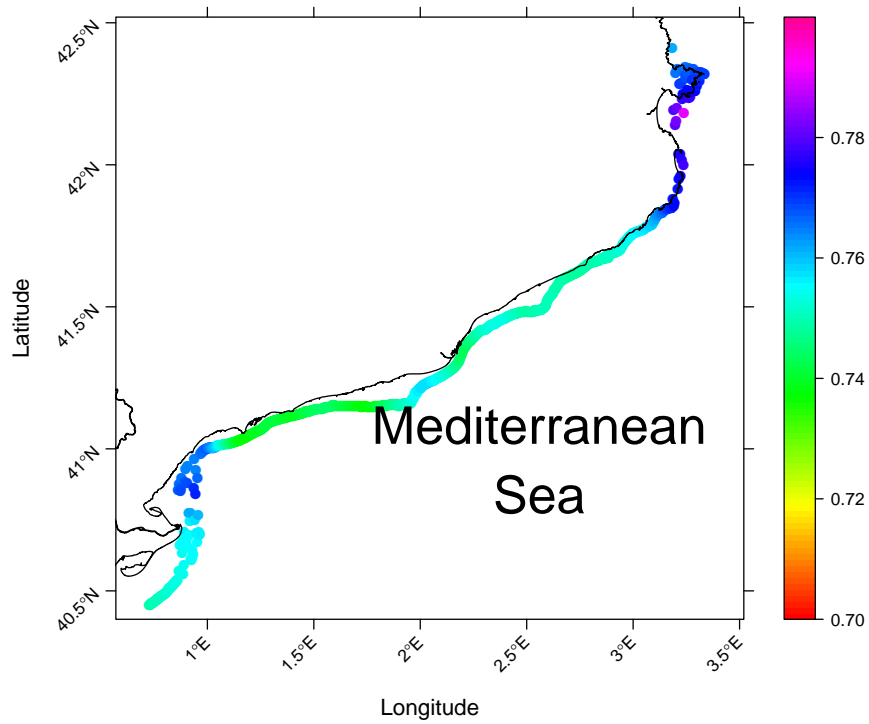


Figure 8: Spatial distribution of the Kendall's rank correlation coefficient ( $\tau$ ) between  $E$  and  $D$  ( $\tau_{(E,D)}$ ).  $\tau \in [0, 1]$ , where 0 is total independence and 1 is total dependence.

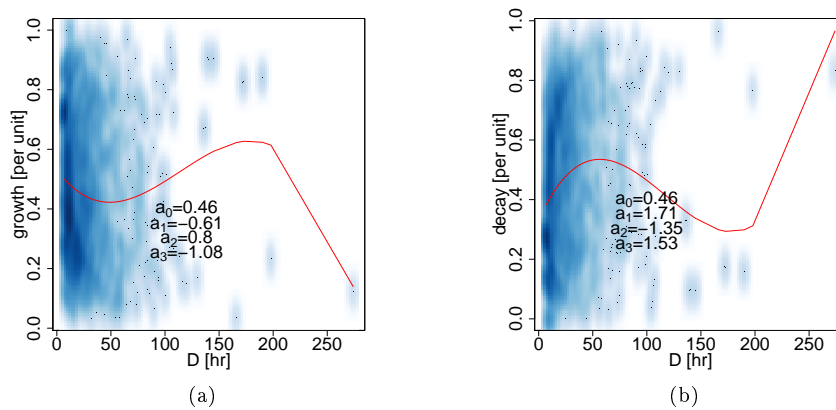


Figure 10: Heat map of a) dimensionless growth-rate vs.  $D$ , and b) decay-rate vs.  $D$ , at node C3. Greater density is represented by darker blue colour.

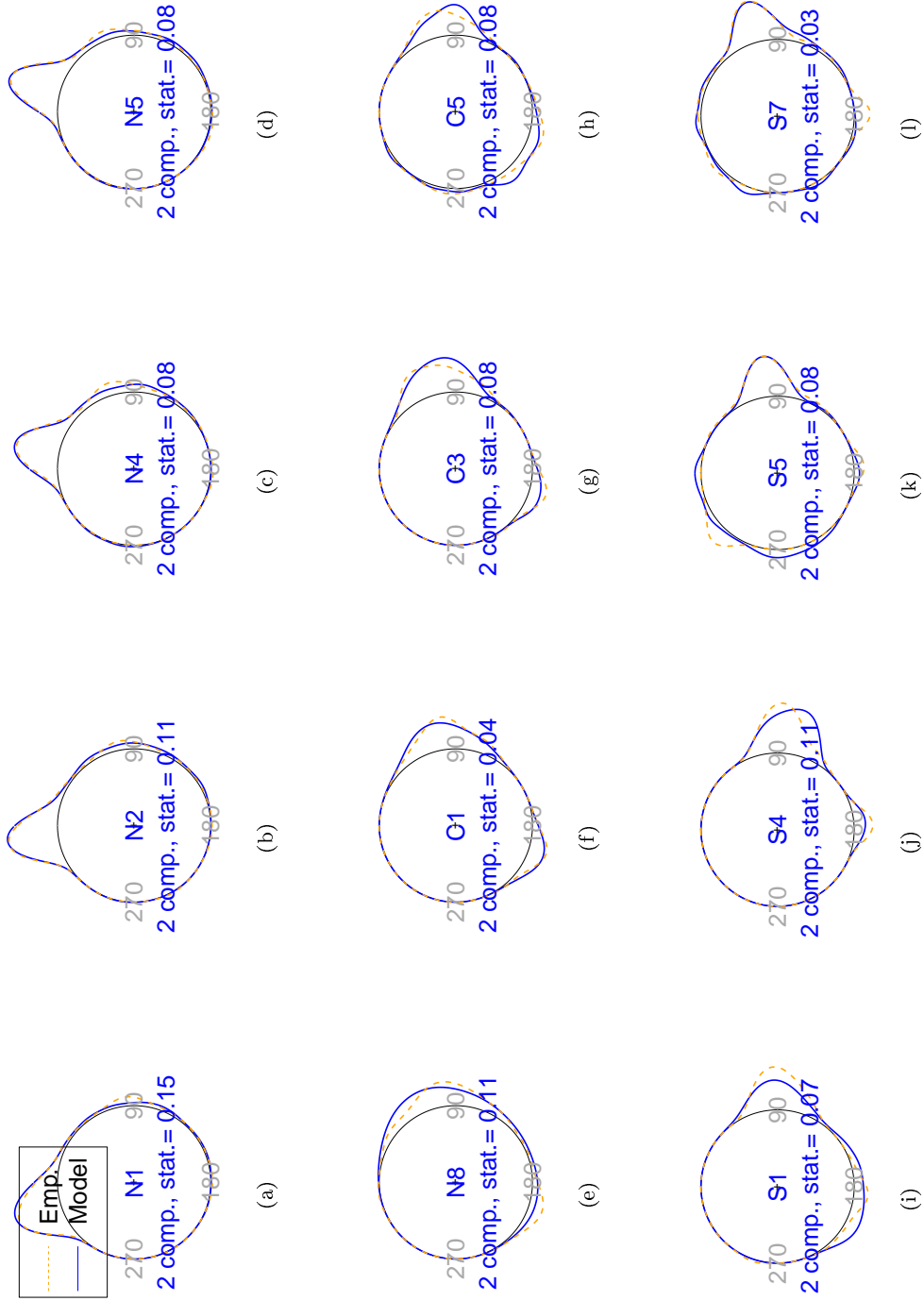


Figure 9: Fitting of movM distributions to  $\theta_p^*$ . In dotted orange, the empirical distribution for each node; in continuous blue, the same for the movM distributions. The node name, the number of movM components and the value of the  $U^2$  statistic are shown, for each node. The North is in the upper part of the directional distribution and the wave directions follow the Nautical convention.

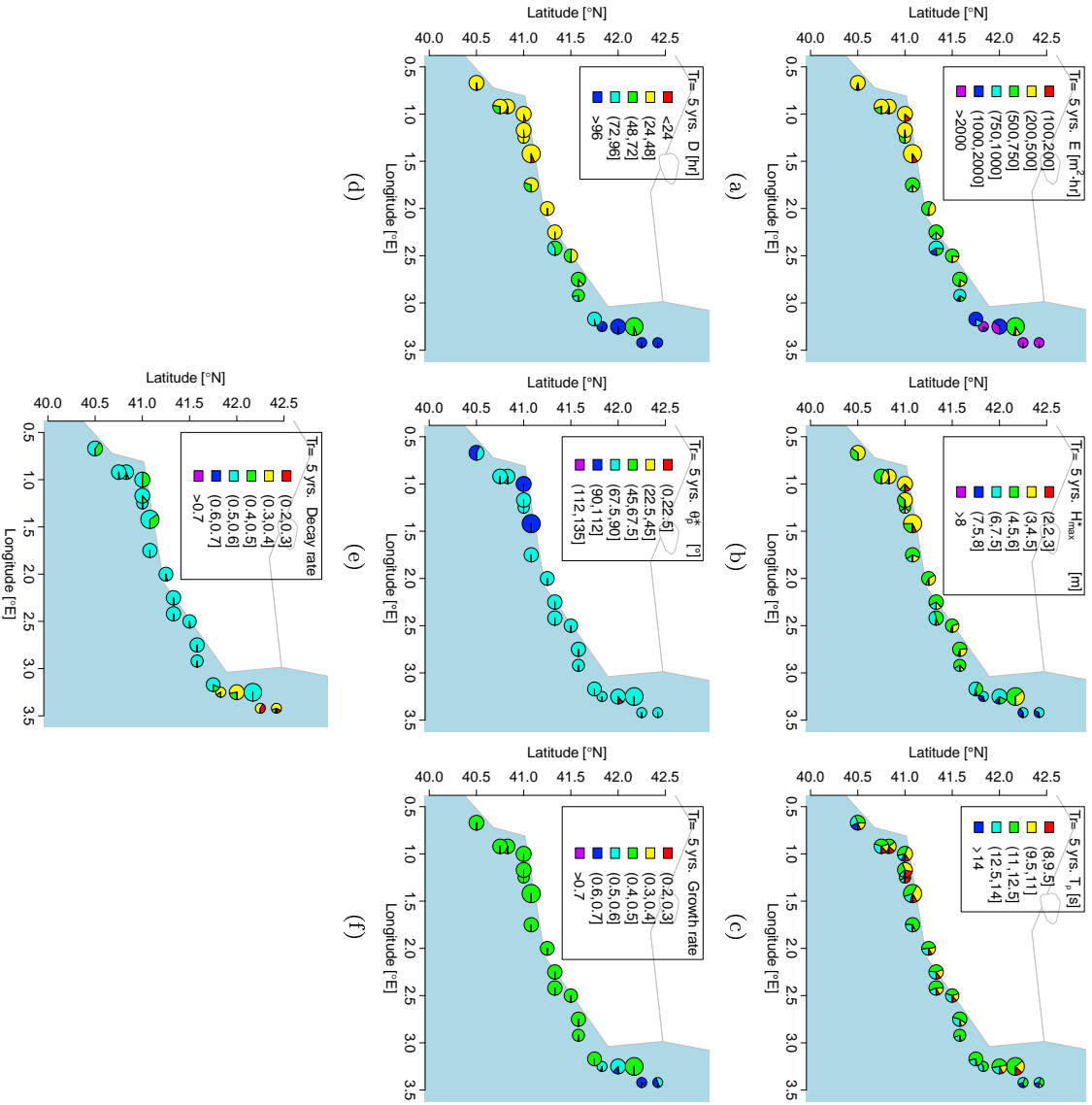


Figure 15: Storm components predicted by the proposed model, for  $T_p$  of 5years, and at each studied node: a) energy ( $E$ ), b) maximum wave-height ( $H_{\max}$ ), c) peak-period ( $T_p$ ), d) duration ( $D$ ), e) wave-direction at peak ( $\theta_p^*$ ), f) growth-rate, and g) decay-rate. Pie-charts represents the frequency of a subset of intervals for each storm component.

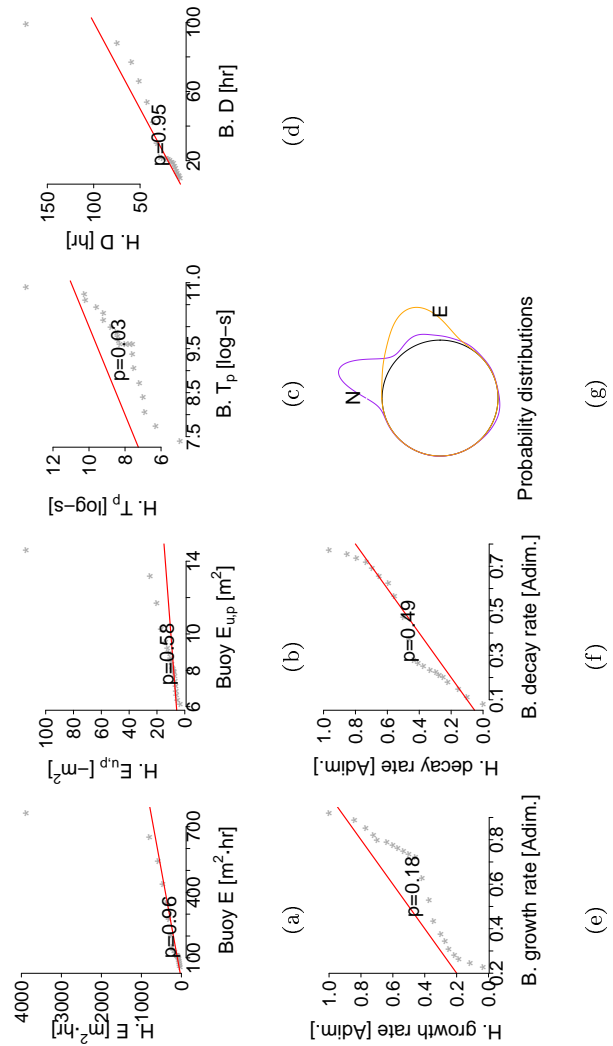


Figure 11: Q-Q plots of PdE-Palamos buoy vs. the SIMAR node N5. The x-axis is buoy data, and the y-axis is the hindcasted data (SIMAR). The orange lines in (g) is the buoy  $\theta_p^*$ , whereas the purple line is the SIMAR  $\theta_p^*$ . The red straight line in the rest of the plots represents the perfect fit. “p” is the p-value, the higher it is, the better the fit.

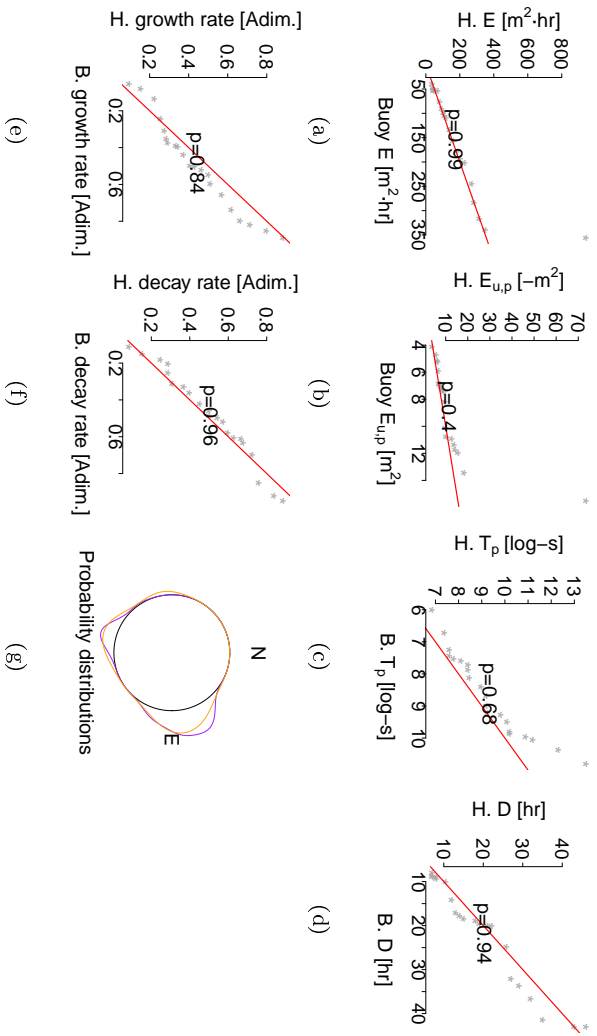


Figure 12: Q-Q plots of PDF-Barcelona-II buoy vs. the SIMAR node C3. The graphs are represented with the same elements (e.g. line colour) than for the PDF-Palamos buoy.



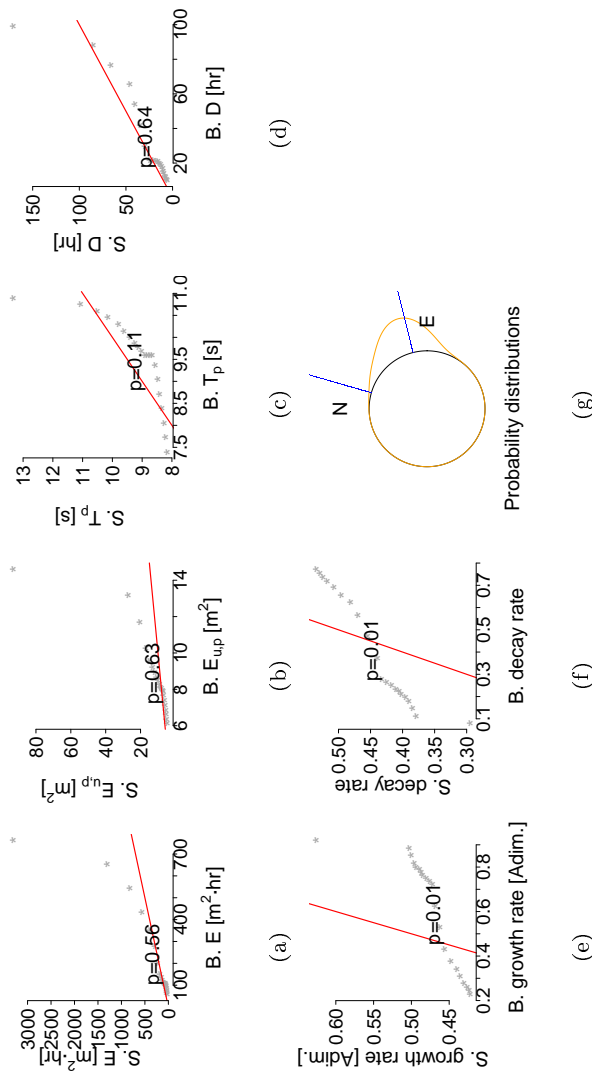


Figure 13: Validation of the node N5 our model by the PdE-Palamos buoy data. The x-axis is the buoy data, and the y-axis is the model generated data. In Fig. g), the blue line represents the model  $\theta_p^*$  and the orange line represents the buoy  $\theta_p^*$ . “p” is the p-value, the highest it is, the better the fit.

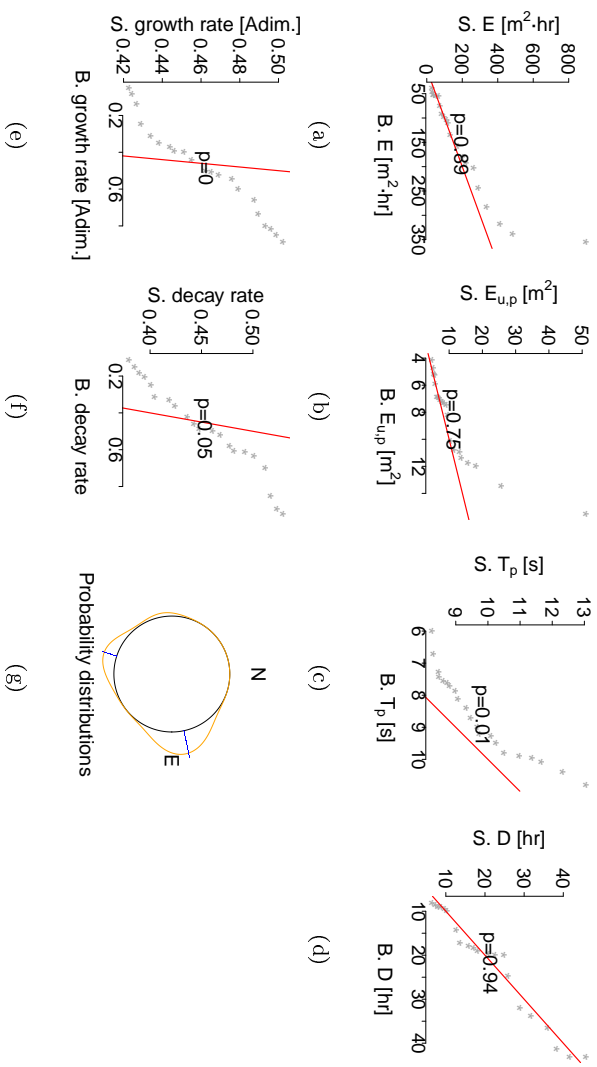


Figure 14: Validation of the node C3 our model by the PDE-Barcelona-II buoy data. Graphs are represented with exactly the same elements (e.g. line colour) than for the N5 case.

Table 1: Buoy location and data availability. All the considered buoys are directional.

Buoy	Longitude (°E)	Latitude (°N)	Depth (m)	Data availability
PdE-Palamos	3.19	41.83	90	26/03/2010 to 30/06/2011
XIOM-Blanes	2.82	41.65	74	13/07/2007 to 31/12/2012
PdE-Barcelona I	2.15	41.29	50	08/03/2004 to 22/12/2013
PdE-Barcelona II	2.20	41.32	68	08/03/2004 to 30/11/2011
XIOM- Llobregat	2.14	41.28	45	05/02/2004 to 31/12/2012
XIOM-Tortosa	0.98	40.72	60	15/06/1990 to 31/12/2012

Table 2: Number of storms per node.

Node	Storms	Node	Storms	Node	Storms	Node	Storms
<b>N1</b>	471	<b>N6</b>	201	<b>C3</b>	75	<b>S3</b>	44
<b>N2</b>	467	<b>N7</b>	134	<b>C4</b>	49	<b>S4</b>	31
<b>N3</b>	88	<b>N8</b>	62	<b>C5</b>	77	<b>S5</b>	59
<b>N4</b>	255	<b>C1</b>	60	<b>S1</b>	42	<b>S6</b>	73
<b>N5</b>	348	<b>C2</b>	99	<b>S2</b>	65	<b>S7</b>	52

Table 3: Parameters of the GPD adjusted to each SIMAR node: location ( $\mu$ ), scale ( $\sigma$ ), and shape ( $\xi$ ). The  $E$  is the storm energy,  $E_{u,p}$  is the maximum unitary storm energy,  $T_p$  is the peak-wave-period associated to  $H_{max}^*$ , and  $D$  is the storm duration. The  $h_0 = 2.2\text{m}$  is the wave height threshold. The  $D_{min} = 6\text{hrs}$  is the required minimum storm duration or duration threshold. The  $T_{min} = 8.17\text{s}$  is the  $T_p$  threshold, obtained from CIIRC (2010).

GPD parameters								
Node	$\log E$ ( $\mu = D_{min} \cdot H_0^2$ )		$\log E_{u,p}$ ( $\mu = H_0^2$ )		$\log T$ ( $\mu = T_{min}$ )		$\log D$ ( $\mu = D_{min}$ )	
	$\sigma$	$\xi$	$\sigma$	$\xi$	$\sigma$	$\xi$	$\sigma$	$\xi$
N1	2.65	-0.54	1.01	-0.34	0.10	-0.00	1.94	-0.50
N2	2.57	-0.52	0.98	-0.32	0.10	-0.02	2.00	-0.57
N3	2.42	-0.72	0.71	-0.30	0.33	-0.79	1.91	-0.76
N4	2.32	-0.50	0.81	-0.24	0.15	-0.24	1.83	-0.54
N5	2.37	-0.48	0.91	-0.27	0.14	-0.23	1.86	-0.55
N6	2.27	-0.55	0.81	-0.24	0.17	-0.29	2.08	-0.76
N7	2.36	-0.63	0.81	-0.26	0.25	-0.53	1.88	-0.72
N8	2.54	-0.75	0.81	-0.27	0.28	-0.53	1.77	-0.68
C1	2.31	-0.68	0.79	-0.25	0.31	-0.59	1.43	-0.56
C2	2.32	-0.61	0.85	-0.24	0.29	-0.61	1.72	-0.62
C3	2.20	-0.62	0.83	-0.25	0.27	-0.48	2.02	-0.99
C4	2.21	-0.64	0.81	-0.22	0.26	-0.47	1.87	-0.90
C5	2.24	-0.63	0.82	-0.24	0.21	-0.34	1.90	-0.87
S1	2.07	-0.76	0.66	-0.22	0.16	-0.12	1.53	-0.75
S2	2.20	-0.68	0.76	-0.25	0.17	-0.21	1.99	-0.95
S3	2.23	-0.76	0.71	-0.25	0.14	-0.08	1.78	-0.86
S4	2.04	-0.74	0.67	-0.23	0.16	0.01	1.99	-1.09
S5	1.87	-0.61	0.64	-0.20	0.28	-0.48	1.50	-0.68
S6	1.87	-0.59	0.68	-0.23	0.24	-0.38	1.45	-0.62
S7	1.64	-0.49	0.65	-0.20	0.16	0.00	1.31	-0.65

Table 4: Parameters of HACs. The selected copula type is Gumbel-HAC, and the aggregation method is “mean”. These parameters can be used to compare different locations.

Node	Tree type	$\theta_{(E,D)}$	$\theta_{((E,D),E_{u,p})}$	$\theta_{root}$	Node	Tree type	$\theta_{(E,D)}$	$\theta_{((E,D),E_{u,p})}$	$\theta_{root}$
N1	A	1.16	2.15	4.44	C3	A	1.27	2.03	3.79
N2	A	1.22	2.23	4.47	C4	A	1.29	1.97	4.17
N3	A	1.14	1.87	4.89	C5	B	1.62		3.54
N4	A	1.27	2.10	4.54	S1	B	1.48		3.74
N5	A	1.45	2.10	4.66	S2	A	1.18	1.81	3.74
N6	B	1.67		4.08	S3	A	1.33	1.92	3.69
N7	B	1.58		3.90	S4	B	1.55		4.30
N8	A	1.43	1.98	3.92	S5	A	1.22	2.01	4.47
C1	A	1.23	1.94	3.95	S6	A	1.29	1.84	4.11
C2	A	1.23	2.03	4.36	S7	A	1.59	2.19	3.89

Table 5: The wave directions at each node derive into pairs of (sin, cos). The set of sines and the set of cosines are characterized by seldom movM distributions. Means ( $\mu$ ) of the movM distributions are provided for each principal direction (PD).

Node	Mean ( $\mu$ ) [°]			Node	Mean ( $\mu$ ) [°]	
	PD1	PD2	PD3		PD1	PD2
<b>N1</b>	344	84		<b>C3</b>	78	198
<b>N2</b>	353	76		<b>C4</b>	81	196
<b>N3</b>	73	353		<b>C5</b>	81	220
<b>N4</b>	11	78		<b>S1</b>	91	195
<b>N5</b>	15	76		<b>S2</b>	85	203
<b>N6</b>	23	88		<b>S3</b>	183	88
<b>N7</b>	74	33	205	<b>S4</b>	94	176
<b>N8</b>	81	200		<b>S5</b>	82	320
<b>C1</b>	84	198		<b>S6</b>	334	77
<b>C2</b>	70	205		<b>S7</b>	74	109

Table 7: Parameters of the function  $f(D) = a_0 + a_1D + a_2D^2 + a_3D^3$ , where  $D$  is storm duration, and  $f(D)$  is either growth or decay-rate.

	growth rate				decay rate			
	$a_0$	$a_1$	$a_2$	$a_3$	$a_0$	$a_1$	$a_2$	$a_3$
N1	0.48	-0.52	0.10	-0.39	0.45	0.85	-0.29	0.51
N2	0.48	-0.48	0.25	-0.57	0.45	1.09	-0.56	0.78
N3	0.48	-0.46	0.24	-0.55	0.45	1.17	-0.62	0.81
N4	0.47	-0.45	0.40	-0.68	0.45	1.35	-0.91	1.07
N5	0.47	-0.52	0.61	-0.82	0.45	1.48	-1.11	1.21
N6	0.47	-0.58	0.67	-0.90	0.45	1.50	-1.15	1.30
N7	0.47	-0.50	0.61	-0.86	0.45	1.47	-1.13	1.31
N8	0.47	-0.47	0.62	-0.89	0.45	1.46	-1.13	1.33
C1	0.47	-0.45	0.61	-0.90	0.45	1.45	-1.12	1.34
C2	0.46	-0.47	0.64	-0.92	0.45	1.47	-1.15	1.36
C3	0.46	-0.47	0.65	-0.94	0.46	1.49	-1.18	1.40
C4	0.46	-0.47	0.65	-0.94	0.46	1.50	-1.19	1.41
C5	0.46	-0.51	0.69	-0.97	0.46	1.56	-1.24	1.46
S1	0.46	-0.52	0.70	-0.98	0.46	1.59	-1.27	1.48
S2	0.46	-0.53	0.71	-1.00	0.46	1.59	-1.27	1.49
S3	0.46	-0.52	0.71	-1.00	0.46	1.61	-1.29	1.52
S4	0.46	-0.52	0.72	-1.02	0.46	1.63	-1.31	1.53
S5	0.46	-0.55	0.75	-1.04	0.46	1.66	-1.33	1.54
S6	0.46	-0.60	0.79	-1.07	0.46	1.70	-1.35	1.55
S7	0.46	-0.61	0.80	-1.08	0.46	1.71	-1.35	1.53

Table 6: Coefficients of the multivariate logit function to predict  $\theta_p^*$  from  $\log E$ ,  $\log E_{u,p}$ ,  $\log T$  and  $\log D$ . If there are three principal direction (PD), the function always uses the most principal component as a reference and displays the prediction for the other components (see column ‘PD#’).

Node	PD#	Intercept	$a_{\log E}$	$a_{\log E_{u,p}}$	$a_{\log T,1}$	$a_{\log T,2}$	$a_{\log T,3}$	$a_{\log D,1}$	$a_{\log D,2}$	$a_{\log D,3}$
N1	2	-1.26	25.38	-63.57	92.02	14.70	-4.37	-21.49	-8.15	3.84
N2	2	-1.10	3.37	-45.61	78.22	13.03	-5.25	-7.70	-10.36	0.96
N3	2	-0.10	-21.12	0.05	-19.67	-0.31	3.74	25.05	-1.53	1.15
N4	2	-0.47	-11.27	5.63	15.35	4.40	-0.57	3.48	0.04	1.80
N5	2	-0.74	-4.10	-8.34	17.40	11.11	0.83	-1.63	-4.04	-1.53
N6	2	-0.34	28.49	-5.24	-0.10	7.76	-0.79	-21.77	-6.14	4.94
N7	2	-0.10	-61.42	17.76	-1.56	0.21	-3.80	45.05	0.46	-0.08
N7	3	-0.99	-63.15	23.87	-13.30	-9.98	-5.55	49.31	-3.11	0.66
N8	2	-1.66	-36.08	12.13	-6.08	-9.84	-8.40	25.42	-3.25	1.99
C1	2	-1.12	-36.46	12.11	1.74	-4.65	2.91	24.59	-1.72	-1.32
C2	2	-1.36	-35.21	13.17	-1.91	-8.35	-1.57	23.79	-5.83	-1.29
C3	2	-1.62	-37.34	12.22	7.13	-9.50	6.30	22.78	-2.36	-6.66
C4	2	-1.77	-6.53	5.34	0.69	-9.34	1.90	4.30	0.40	-3.56
C5	2	-0.19	-21.52	12.48	-16.53	2.32	-14.11	11.23	3.30	-6.14
S1	2	-1.22	21.23	-8.58	-3.61	4.73	-8.45	-16.31	-1.53	-4.63
S2	2	1.05	56.13	-22.29	-29.22	23.29	-10.70	-39.64	3.25	-0.43
S3	2	-1.80	-22.87	14.49	35.72	-29.01	9.78	18.48	3.96	7.55
S4	2	-2.75	26.24	-6.02	-4.28	-5.24	-5.97	-31.02	-13.96	-10.79
S5	2	4.01	40.45	-21.28	-64.86	43.36	-13.80	-35.83	-2.55	-2.51
S6	2	-3.65	-13.77	4.41	60.06	-31.89	15.36	26.01	8.89	9.07
S7	2	3.83	55.13	-17.94	-65.67	50.19	-25.26	-37.77	4.19	2.63